SEISMIC SHEAR-WAVE STRUCTURE OF THE UPPER MANTLE BENEATH THE MOHNS RIDGE

A THESIS SUBMITTED TO THE GRADUATE DIVISION OF THE UNIVERSITY OF HAWAIʻI AT MĀNOA IN PATIAL FULFILLMENT OF THE REQUIREMENTS FOR THE DEGREE OF

MASTER OF SCIENCE

IN

GEOLOGY & GEOPHYSICS

AUGUST 2011

By
Michaela M. Conley

Thesis Committee:

Robert A. Dunn, *Chairperson*
Frederick K. Duennebier
Cecily J. Wolfe

Keywords: Mohns Ridge, very-slow spreading, thin crust, 1D seismic velocity model

ACKNOWLEDGEMENTS

All maps are produced using GMT software [*Wessel and Smith*, 1998]. All JMI and JMIC data and instrument responses come courtesy of NORSAR (http://www.norsar.no). Initial data processing was performed using the software package SAC [*Goldstein*, 1996]. Thanks to Eric Hellebrand, Garrett Ito, Rolf Mjelde, and John Sinton for very helpful conversations. Thanks to Rob Dunn, Fred Duennebier, Cecily Wolfe, and John Sinton for their helpful comments regarding this manuscript. This research was supported by NSF grant OCE0648507.

I wish to say a very special "thank you" to my friends (David Gandy, Ásdís Benediktsdóttir, and Ashley Hampton to name a few) and my family. Without your support and encouragement I would never have been able to complete this journey.

ABSTRACT

Crust produced at mid-ocean ridges with full spreading rates less than ~20 mm/yr is observed to be only 0-4 km thick, well below the global average of 6-7 km for oceanic crust produced at faster spreading rates. The origin of this difference is unknown, but is speculated to result from a thicker thermal boundary layer at the axis of the slower spreading ridges that either inhibits shallow melting or melt extraction. We present an analysis of regional broadband data, predominately Love and Rayleigh waves, collected along the very slow-spreading Mohns Ridge (where crustal thickness is ~4 km) in the Norwegian-Greenland Sea. The seismic data constrain lithospheric and asthenospheric velocities for lithospheric ages from 0-25 Ma. We find lithospheric thickness to closely match the prediction of a simple ridge half-space thermal model (via the temperature and pressure effects on the seismic properties of mantle materials) and asthenospheric shear wave velocities to be consistent with this thermal model plus <2% melt at the youngest ages. Just at the top of the mantle, a thin zone with velocities intermediate between those of mantle and gabbroic rocks suggests that some melt is frozen into the mantle as might occur if a thin axial lithospheric lid inhibits melt extraction from the mantle and the melt is subsequently frozen into the mantle. While this explains the thin crust, the possibility that hydrothermal alteration produces the low mantle velocities cannot be ruled out.

TABLE OF CONTENTS

LIST OF TABLES

LIST OF FIGURES

CHAPTER 1. INTRODUCTION

While regional waveform studies from the Pacific to the Atlantic (e.g., *Nishimura and Forsyth* [1989], *Xu and Wiens* [1997], *Gaherty* [2001], *Dunn and Forsyth* [2003], *Gu et al.* [2005], *Wiens et al.* [2006], *Delorey et al.* [2007], and *Gaherty and Dunn* [2007]) constrain the seismic structure of the upper mantle for mid-ocean ridges with full spreading rates greater than 20 mm/yr, few studies of this nature exist for mid-ocean ridges spreading at rates less than 20 mm/yr. Despite the lack of mantle seismic studies for these very slow spreading ridges, over the past decade much has been learned about this relatively new class of mid-ocean ridge. Ridges in this category display linked magmatic and amagmatic accretionary segments, a lack of transform faults, exposed mantle on the seafloor, and anomalously thin crust [*Dick et al.*, 2003]. Measured crustal thicknesses range from 0-4 km, well below the 6-7 km global average for oceanic crustal thickness [*Bown and White*, 1994]. Abnormally thin crust has been discovered at the Gakkel Ridge [*Jackson et al.*, 1982; *Michael et al.*, 2003], the South-West Indian Ridge [*Muller et al.*, 1997], the Knipovich Ridge [*Ritzmann et al.*, 2002] and the Mohns Ridge [*Klingelhöfer et al.*, 2000a]. For some sections of these ridges, the melt supply is suspected to at least temporarily drop to zero, resulting in the direct emplacement of mantle at the seafloor [e.g., *Dick et al.*, 2003]. The process of crustal production at mid-ocean ridges and other spreading centers is fundamental to our understanding of mantle dynamics and melting and this observed spreading rate dependence on crustal production at very slow spreading rates indicates a fundamental change in sub-ridge processes.

At present, there are two end-member hypotheses to explain the reduced crustal production at very slow spreading ridges. While each emphasizes the importance of a thermal lid on controlling sub-ridge mantle processes, one suggests that the thermal lid suppresses melting while the other posits that it inhibits melt migration. In the melting-suppression model [*Reid and Jackson*, 1981] the sub-axial thermal structure is governed by conductive cooling and in very-slow spreading environments a thick thermal boundary layer forms at the ridge axis. This shuts off melting at the top of the melting column at deeper depths than is predicted to occur for faster spreading ridges and, all else being equal, reduces the overall amount of melt produced in the mantle **(Figure 1)**. Numerical calculations [e.g., *Reid and Jackson*, 1981; *Bown and White*, 1994; *Niu and Hekinian*,

1997] predict that melting shuts off at a depth of 30 km or more below the crust for the slowest spreading ridges. The global three-dimensional S-wave velocity model of *Zhang and Tanimoto* [1992] has been interpreted to support the thick lithosphere theory [*Niu and Hekinian*, 1997]. Averaged S-wave velocity variations plotted as a function of spreading rate indicate that slower spreading ridges are underlain by seismically faster material at depths ≤36 km. This increase in velocity can be interpreted as thicker lithosphere directly beneath the axis of slower spreading ridges as compared to faster spreading ridges, although the lateral resolution of the study at the ridge axis is poor.

In the inhibited-migration model [*Cannat*, 1996] melt production is normal but melt transport through the lithosphere is at least partially inhibited. This model does not require an exceptionally thick lithosphere along the ridge, but only a slightly thickened lithosphere. The thickened lithosphere causes mantle melts migrating to the surface to become trapped and frozen beneath the crust; the final crustal thickness therefore does not represent the total amount of melt produced within the mantle. For example if the thickness of magma produced by the mantle 6 km and the mantle lithosphere is 6 km thick at the ridge with 50% of the material composed of entrapped melt, then the final crustal thickness will be only 3 km.

These two hypotheses are observationally testable, and distinguishing between them can provide significant information on mantle dynamics beneath mid-ocean ridges. To help distinguish between them, we performed a detailed regional waveform study of the upper mantle seismic structure beneath the Mohns Ridge, a very slow spreading ridge with anomalously thin crust. By means of a joint inversion using both Love and Rayleigh waves, we developed lithospheric age-dependent velocity models of the Mohns Ridge. These models constrain the thickness and shear wave velocity of the lithosphere, asthenospheric velocities, and mantle anisotropy. The results are compared to a prediction derived from a thermal cooling model and to similarly determined seismic models from the north Atlantic and the Pacific.

CHAPTER 2. GEOLOGIC SETTING

The Mohns Ridge **(Figure 2a)** is centrally located in the Norwegian-Greenland Sea and is obliquely spreading at a full rate of 16 mm/yr [*Vogt*, 1986; *Kreemer et al.*, 2003; *Muller et al.*, 2008]. The location of the ridge axis has remained relatively stable since its formation ~60 Ma [*Talwani and Eldholm*, 1977] thus resulting in nearly symmetric spreading. The strike of the ridge is 60° from north and its length is about 580 km.

An active-source seismic refraction and gravity study that sampled crust produced at the Mohns Ridge over the age range of 0-22 Ma, has discovered anomalously thin crust with a mean thickness of 4.0±0.5 km [*Klingelhöfer et al.*, 2000a]. The thin crust results from a very thin, underdeveloped, lower crustal layer (seismic layer 3) that is often interpreted to be composed of gabbros. The authors do not rule out that layer 3 may be at least partially composed of serpentinized mantle rocks. The mantle immediately beneath the crust exhibits unusually low P-wave velocities, ~7.5 km/s on average, and as low as 7.2 km/s along a ridge-parallel seismic profile located within the rift valley; the depth to which these low velocities penetrate is not well constrained. The authors suggest that faults and fractures, along which seawater penetrates, may reach greater depths than for faster spreading ridges, with the result that fluids chemically alter (serpentinize) the upper mantle and lower the bulk seismic velocity. An alternative or additional explanation provided is that the alignment of the fast-axes of olivine in the flow direction away from the ridge results in a lowering of the seismic wave speed along their ridge-parallel seismic profiles.

Water depth along the Mohns Ridge ranges from ~2.8 km at the southern end to ~3.2 km at the northern end [*Géli et al.*, 1994]. The anomalously shallow southern end of the ridge is thought to result from a melting anomaly suggested by some to be the result of interaction of the ridge with a hotspot [*Talwani and Eldholm*, 1977; *Vogt et al.*, 1981]. Possible evidence for such interaction comes from a regional tomographic study [*Pilidou et al.,* 2004; 2005] revealing S_v-wave velocities at 100-300 km depth that vary along the ridge with relatively lower velocities towards the southwestern end of the ridge and higher velocities towards the northeastern end. The anomalous structure may result from

an interaction with the Iceland hotspot, but the existence of a unique plume beneath Jan Mayen has also been speculated [*Neumann and Schilling*, 1984; *Schilling*, 1985; *Pilidou et al.*, 2004; 2005].

Geochemical analyses of Mohns Ridge lavas show variable incompatible element enrichments unique to the area [*Haase et al.*, 1996; *Schilling et al.*, 1999; *Hanan et al.*, 2000]. Also, selected isotopic ratios, such as $^{87}Sr/^{86}Sr$ and $^{206}Pb/^{204}Pb$, trend from higher values at the southwestern end of the Mohns Ridge towards lower values at the northeastern end [*Schilling et al.*, 1999; *Hanan et al.*, 2000] and can be interpreted as an indicator of hotspot influence near Jan Mayen. A rare earth element (REE) inversion assuming a primitive mantle yields a melt thickness, and equivalent crustal thickness, of 5.9 km [*Klingelhöfer et al.*, 2000b]. Because the evidence supporting a Jan Mayen mantle plume is controversial [*Haase et al.*, 1996], *Klingelhöfer et al.* [2000b] prefer the results of an additional REE inversion assuming mantle with an average ε_{Nd} (measured $^{143}Nd/^{144}Nd$ ratio) of 7.0, as observed for Mohns Ridge basalts, that indicates melt production with an equivalent crustal thickness of ~5 km. This thickness corresponds well with melt production inferred from Na concentrations corrected for fractionation [*Klingelhöfer et al.*, 2000b]; however, the associated errors range from 0.5-1.0 km. The discrepancy between the geochemically-derived thickness and seismically-derived thickness is ~1 km (i.e., close to, but at the limits of, the uncertainty in the results).

CHAPTER 3. DATA

This study utilizes data from 27 earthquakes located along the Mohns and Knipovich ridges **(Figure 2b)**. Source mechanisms predominantly indicate normal faulting with the direction of extension approximately parallel to the direction of spreading; only those events whose back azimuth do not lie along a node in the radiation pattern were used. Events range in magnitude from M_w 4-6 with source-to-receiver distances from 90 km to 950 km for the furthest Knipovich Ridge events. The data were recorded on broadband stations JMIC (operational from 10/31/2003 – present) and its predecessor JMI (operational from 8/31/1994 – 10/31/2003). Both stations employed Streckeisen STS-2 instruments owned and operated by Norwegian research groups, and waveform data are publicly available via the NORSAR and IRIS databases. These stations are ideally situated for studying Mohns Ridge mantle structure because of their location on Jan Mayen Island near the southern end of the ridge.

Each seismic trace was initially cut to 120 s before and 120 s after the expected S-wave arrival time and the horizontal data were rotated to obtain radial and transverse waveforms; all data were corrected for instrument response. JMI data prior to October 2001 were corrected for a north/east channel swap problem while all JMI data were corrected for a 16° (azimuthal) instrument misalignment. Vertical and transverse broad band-pass filtered data sorted by epicentral distance are shown in **Figure 3**; strong surface wave arrivals for both Rayleigh and Love waves are clearly observed in the data. For waveform modeling, fundamental mode wavelets of Love and Rayleigh waves, centered about a given period, were extracted by narrow band-pass filtering the data as discussed below.

CHAPTER 4. METHODS

The data were divided into three sets to model mantle structure for the following lithospheric age ranges: 0-5 Ma, 5-15 Ma, and 15-25 Ma. We solved for an average one-dimensional (depth varying) velocity profile for each age range. The 19 earthquakes distributed along the Mohns Ridge were used to invert for the near axis (0-5 Ma) seismic velocity profile while a total of 8 earthquakes (4 per age range) located along the Knipovich Ridge constrained the 5-15 Ma and the 15-25 Ma velocity profiles. Seismic wave paths for the 15-25 Ma group traverse lithosphere of variable age, up to ~50 Ma, and as such may not accurately represent 15-25 Ma lithosphere. Nonetheless, the average age of the lithosphere traversed by the waves lies within the given age limits. Synthetic seismograms were calculated using a reflectivity code based on the method of *Randall* [1994] as modified by *Xu and Wiens* [1997] to include a water layer. The reflectivity method calculates the waveforms for both body and surface waves therefore eliminating the difficult task of separating the body wave arrivals from the surface wave arrivals at small source-to-receiver offsets. The reflectivity method requires the basic event parameters and moment tensor, along with 1-D models of P-wave velocities, S-wave velocities, and density. Before beginning the modeling, we verified the waveform code by comparing its output against known solutions for simple seismic structures.

For the 0-5 Ma age range, the initial S-wave velocity model used to start the data modeling **(Table 1)** was determined by first computing a basic half-space cooling model for oceanic lithosphere (with a crust-mantle interface temperature of 650ºC and mantle potential temperature of 1300ºC) [e.g., *Turcotte and Schubert*, 2002] and then converting this to a seismic model using the methods of *Faul and Jackson* [2005]. A single profile is determined by laterally averaging the model over the 0-5 Ma age. The *Faul and Jackson* method accounts for the temperature and pressure effects on mantle minerals, but neglects the possible effect of melt in the asthenosphere. Their method is also frequency dependent and we averaged the results over the appropriate frequency range for the data. The mantle P-wave velocity was set to 1.8 times the S-wave velocity. For the crust, values were taken from the results of a local active source seismic study [*Klingelhöfer et al.*, 2000a]. The starting velocity model for the 5-15 Ma age group was the final solution

for the 0-5 Ma age group, and the starting model for the 15-25 Ma age group was the solution for the 5-15 Ma age group.

Synthetic seismograms in the vertical and transverse directions were narrow band-pass filtered in the same manner as the data. A Gaussian shaped filter was used with thirteen center periods for Rayleigh wave (15, 18, 22, 26, 30, 34, 42, 50, and 65 s) and Love waves (9, 11, 14, 17, 20, 24, 29, 34, and 40 s). In the frequency domain, the filter is of the form $F(w) = \exp\left(-\frac{(w-w_0)^2}{2\gamma^2}\right)$ where w is frequency in radians, and the filter width, γ, ranged from roughly 0.02-0.03, depending on the center frequency, w_0. The amplitudes of the wavelets were normalized by their standard deviations to minimize any effects of the uncertainty in the instrument response (particularly station JMI), the seismic moment, and the earthquake depth.

Direct comparison of filtered synthetic and observed waveforms via a computed misfit value (the mean absolute difference between the synthetic and observed seismograms) determined goodness of fit. In order to down weight the importance of waveforms with low signal-to-noise ratios, the misfit for each wavelet was divided by a weighting factor, or relative waveform uncertainty. The weighting factor was calculated as the mean absolute difference between the observed wavelet and a theoretical (noise-free) wavelet with the same center period and phase. The radial component data yielded waveform uncertainties significantly larger than the other two components and were eliminated from the analysis. A few individual wavelets with very low signal-to-noise ratios were also removed. To account for crustal thickness and water depth variations along the great-circle paths, surface wave phase corrections were calculated [*Bozdag and Trampert*, 2008] and applied to the synthetic data resulting in a more accurate representation of the observed data (i.e., improved misfit).

The inversion was preformed using an iterative grid search method over the velocity layers of the lower crust and the upper mantle. The search began at the top of the model and moved downward over 13 velocity layers to ~200 km depth. On the basis of a sensitivity analysis, the model below ~200 km depth and within the uppermost crust has negligible influence on the data and was not perturbed during the inversion. A smoothness constraint was applied with each iteration to avoid any spurious

perturbations. Initially, only longer period data were included; shorter-period data were added as the model misfit improved. An obvious discrepancy between Rayleigh and Love data indicated the presence of anisotropy ($V_{SH} > V_{SV}$) which is often detected beneath mid-ocean ridges and is generally attributed to the horizontal alignment of the a-axis of olivine crystals due to shear deformation via mantle flow [e.g., *Nishimura and Forsyth*, 1989]. Radial anisotropy was included in the mantle portion of the model and the values were determined as part of the iterative scheme. Although crustal anisotropy is possible along mid-ocean ridges [e.g., *Dunn et al.*, 2001], allowing anisotropy in the crust did not yield a significant improvement of the data misfit and was not included in the final results.

CHAPTER 5. RESULTS

The final solution of the anisotropic 1-D velocity profile for each age range is shown in **Figure 4** and waveform fits for several periods and events are shown in **Figure 5**. The data misfit as a function of period is shown in **Figure 6a** for the starting model and **Figure 6b** for the final model (0-5 Ma). At each age range, a prominent high-velocity lithospheric lid is present at the top of the mantle. The thickness of the lithospheric lid is least for the 0-5 Ma profile and thereafter increases substantially with lithospheric age. Beneath the lithospheric lid, shear wave velocities decrease with depth forming an upper mantle asthenospheric low-velocity region.

A notable feature of each of the three profiles is a region of **A**nomalous **L**ow **V**elocities **IN** (ALVIN) the upper mantle just beneath the base of the crust. The ALVIN region is ~7 km thick with average shear wave velocities of ~4.0-4.4 km/s. Shear wave values at the oldest ranges are slightly faster than those at the youngest age range, however this age-related difference is only weakly supported by the data. In general these shear wave values are less than expected for typical oceanic lithosphere (which can be 4.5 km/s or more), but in line with those estimated from the local refraction experiment of *Klingelhöfer et al.* [2000a].

Sensitivity tests were performed to determine to what extent the ALVIN region is required by the data. The ALVIN region was a persistent feature of all solutions to the problem irrespective of starting model, smoothness constraints, anisotropy, or assumption about the thickness or velocity of the crust. For example if the upper layers of the mantle were artificially held at 4.5 km/s, to coincide with the fastest lithospheric layer, the data misfit increased significantly, particularly for the shorter period data and a discrepancy between Rayleigh and Love phase fits formed. The tests do show some trade-off between the velocity of the layers within the ALVIN region and the ALVIN region's thickness as well as a trade-off with velocities just above or below it. While model uncertainties are difficult to obtain with this type of experiment, we estimate roughly a 2 km uncertainty in the ALVIN thickness and 0.2 km/s uncertainty in the shear wave speed.

The 0-5 Ma age range exhibits a mantle anisotropy of roughly 6% ($V_{SH} > V_{SV}$; anisotropy is defined here as $\frac{V_{SH} - V_{SV}}{V_S}$) in the top 20 km of the mantle that decreases at greater depths. As compared to a purely isotropic solution, the anisotropic solution removes a discrepancy between the data fits of the Rayleigh versus the Love data and the overall misfit drops by 13%. As compared to the 0-5 Ma age range, the older age ranges exhibit lower degrees of anisotropy, with peak values near 4.5%. We note however that the great circle ray paths for the older age ranges are oblique to the axis of the Mohns Ridge and azimuthal anisotropy (with the olivine a-axis parallel to the spreading direction) may reduce the Love-Rayleigh discrepancy that gives rise to our radial anisotropic result. Sensitivity tests show that below ~150 km depth, the data are not sensitive to changes in anisotropy. For this test cosine tapers were applied to the bottom of the anisotropy model over a range of depths to determine to what depth the data were no longer sensitive to anisotropy.

The sensitivity of the results to crustal thickness is an important issue. While we assume the average crustal thickness along the ray paths is 4.2 km on the basis of the *Klingelhöfer et al.*, [2000a] refraction study, the actual crustal thickness along the paths may be different. For example, seafloor bathymetry suggests thicker crust to the south, near the stations, and much thinner crust at the northern end of the Mohns Ridge. As noted above, the effect of crustal thickness changes was corrected for in the synthetic data. This was done by first assuming 4.2 km thickness for the central portion of the Mohns ridge and then using seafloor bathymetry and an isostasy argument to predict crustal thickness elsewhere along the ray paths. Given the predicted thickness difference relative to 4.2 km, we calculated the accumulated phase changes due to the crustal thickness variation [*Bozdag and Trampert*, 2008] and added the result to the synthetic data. While this reduced the overall misfit, there is no assurance that the synthetics are corrected to the proper average crustal thickness. Therefore the sensitivity of the seismic profiles to changes in average crustal thickness was tested by increasing and decreasing the thickness of the lower crust. The results of the tests indicate that while there is some trade-off between the crustal thickness and velocities both above and below the base of the crust, unknown crustal thickness variations are not likely to explain away the ALVIN

region itself. As an example, a 6 km thick crust produces significantly higher misfits relative to the model with a 4.2 km thick crust, particularly affecting shorter periods where misfits in wavelet phase approach $\pi/2$ **(Figure 6c)**.

The sensitivity of the data to the thickness of the high-velocity lithospheric lid was also examined. For the 0-5 Ma age range, the thickness was increased by 6 and 12 km over that shown in **Figure 4a**. The first case resulted in slightly higher misfit values (2.3%) and early arrivals of 1-1.5 sec on average for the 14-40 sec Love data and the 15-30 sec Rayleigh data. The second case produced similar results; misfit values increased by 10.75% and arrivals were 2-2.5 sec on average too early for the same periods **(Figure 6d)**. The misfit increases more rapidly if the lithosphere is thinned rather than thickened. Again, while it is difficult to place absolute bounds on model values, the data show enough sensitivity to lithospheric thickness that we suggest that our final model is close to having the appropriate average lithospheric values for the given age range.

CHAPTER 6. INTERPRETATION AND IMPLICATIONS

Figure 7 shows the final V_{SV} models for the three age ranges as compared to other velocity models of the same age: the *Faul and Jackson* [2005] prediction based on a half-space cooling model and the effects of thermal structure and pressure on mantle materials, the *Nishimura and Forsyth* [1989] model for the Pacific, and the *Delorey et al.* [2007] model for the northern Atlantic Ocean and Reykjanes Ridge. In **Figure 7**, all model depths are referenced to the base of the crust. At the oldest age range, the Mohns (apart from the ALVIN region) and Pacific models agree with the half-space cooling model, suggesting no significant effect from ridge-related mantle melting or other influences. At the 5-15 Ma age range the Mohns model has slightly lower sub-lithospheric velocities than predicted by the simple cooling model, perhaps indicating the addition of a small amount of melt originating from ridge-related upwelling and decompression melting. At the 0-5 Ma age range, the data-derived models all deviate from the simple cooling model, as is expected for the presence of melt in the upwelling region. For the Mohns model, <2% melt [e.g., *Schmeling*, 1985] can explain the observed discrepancy at 0-5 Ma and <1% melt can explain the discrepancy at the 5-15 Ma age range. Below 60 km depth, the Mohns mantle has faster shear wave velocities than for either the Pacific [*Nishimura and Forsyth*, 1989] or Reykjanes [*Delorey et al.*, 2007] models and is similar to the estimate from the half-space cooling model. In addition, the velocities below 60 km depth do not increase with distance from the ridge axis (or more accurately, the data do not require such an increase) and thus there is no obvious upwelling-related anomaly below this depth. While we cannot rule out melt at depths below 60 km, any upwelling-related melting that may take place occurs in undetectable quantities. The Reykjanes model deviates the most from the thermal model predictions and is suggestive of a broad and deep region of melt and melting that may result from the influence of the Iceland hotspot [*Delorey et al.*, 2007]. The Mohns ridge seismic structure does not suggest a similar influence from Iceland [*Talwani and Eldholm*, 1977; *Vogt et al.*, 1981] or the proposed Jan Mayen hotspot [*Neumann and Schilling*, 1984; *Schilling*, 1985].

At very slow spreading rates it has been suggested that deeper, more pervasive fracturing of the crust enhances hydrothermal cooling [*Francis*, 1981] leading to a considerably thicker lithosphere than predicted by conductive cooling models. Our results do not substantiate this idea. The Mohns Ridge velocity structure for the 0-5 Ma age range **(Figure 7a)** is consistent with "normal" thickness lithosphere as predicted by the conductive cooling models. If we define the base of the lithosphere as the depth of maximum negative gradient of the velocity (e.g., *Gu et al.*, [2005]), then the Mohns Ridge velocity model suggests a lithospheric thickness of ~22-34 km, neglecting the crust. The thickness of the mantle lithosphere predicted by the half-space cooling model is ~25 km averaged over this age range. Lithospheric thicknesses estimated for the older age ranges also agree well with the theoretical calculation. Although the data do not sample in detail the axis of the ridge, the thickness of the mantle lithosphere at the ridge axis is estimated to be <10 km on the basis of the off-axis profiles and extrapolation of conductive cooling isotherms back to the ridge axis. In addition, gravity data indicate the presence of a low-density region in the lower crust beneath the ridge axis [*Géli et al*., 1994] and seismic wave speeds in the axial lower crust and mantle are lower than away from the ridge axis [*Klingelhöfer et al.*, 2000a]. These observations indicate that lower crustal temperatures at the ridge axis are high and support the idea that the axial lithosphere is not unduly thick.

Irrespective of whether deep hydrothermal cooling occurs, several models have been developed to show that at the slowest spreading rates a decrease in melting occurs at shallow depths as a result of conductive cooling of the sub-ridge mantle [e.g., *Reid and Jackson*, 1981; *Bown and White*, 1994; *Niu and Hekinian*, 1997]. In these models a thicker mantle lithosphere results in a shorter melting column beneath the ridge and thus an overall thinner crust than for faster spreading ridges. Such a process might explain the difference between the thickness of typical mid-ocean ridge crust at faster spreading rates (6-7 km) and the geochemically estimated thickness of the column of melt produced beneath the Mohns Ridge (~4.5-5.9 km) [*Klingelhöfer et al.*, 2000b]. However, there are some problems with this hypothesis. For example, the ~0.5-2 km disagreement between the geochemical estimate of the amount of melt produced and the seismic estimate of the crustal thickness. Furthermore, this hypothesis ignores melt transport and how mantle

melts would pass through such a thick axial lithosphere. It also ignores whether melts freeze within the conductively cooled mantle lid and whether the heat released would inhibit deepening of the lithospheric-asthenospheric boundary (i.e., work against a deep cooling process).

We suggest that while some inhibition of *melting* may occur beneath the Mohns Ridge as predicted by the conductive cooling argument, a large portion of the 'missing' melt is frozen into the uppermost mantle **(Figure 8)** forming the observed ALVIN region with its shear wave velocities that are intermediate between mantle and crust. Assuming a gabbro velocity of 3.8 km/s and a mantle velocity of 4.5 km/s, ~35% gabbroic material in the mantle would explain the velocities within the ALVIN region. This corresponds well with a crust that is ~2-3 km thinner than the average mid-ocean ridge crust of 6-7 km.

In addition to the Mohns Ridge, anomalously low sub-crustal seismic velocities (ALVIN-like regions) have been documented for the Gakkel Ridge [*Jokat et al.*, 2003] and part of the western North Atlantic with very-slow paleo-spreading rates [*Lizarralde et al.*, 2004] thus suggesting that an ALVIN-like region may be a common feature of very-slow/ultraslow spreading regimes. The explanation for these ALVIN-like regions is debated with some favoring serpentinization of the upper mantle [*Klingelhöfer et al.*, 2000a; *Jokat et al.*, 2003] and others favoring melt retention in the upper mantle [*Lizarralde et al.*, 2004]. Although these two scenarios are seismically indistinguishable, we favor the melt retention interpretation for the following reasons: (1) Geochemical models predict greater melt production than what is determined by the thickness of the crust [*Klingelhöfer et al.*, 2000b]. Perhaps this excess melt is trapped in the mantle. (2) The deep penetration of hydrothermal cooling would result in an unusually thick lithosphere, which is not supported by the Mohns seismic model. (3) At very slow spreading rates the brittle-ductile transition is in the mantle, rather than in the crust, and steady state magma chambers are not likely to be present [*Phipps Morgan and Chen*, 1993]. This means that melts ascending from the mantle may become trapped beneath a sub-crustal permeability barrier and it seems likely that at least some of these melts would freeze into the uppermost mantle. (4) The pressure limitations on the depth of fluid penetration [*Phipps Morgan and Chen*, 1993] and volume expansion associated with hydrated olivine effectively seals fractures, restricting deep fluid flow into the mantle

[*Schroeder et al.*, 2002]. A combination of some mantle alteration and 'crustal emplacement' to explain the presence of the ALVIN region cannot be ruled out.

CHAPTER 7. CONCLUSIONS

1. Lithosphere thickness extending away from the Mohns Ridge, as deduced from broadband seismic data and modeling, is consistent with a normal oceanic half-space cooling model.

2. Asthenospheric velocities near the Mohns Ridge are consistent with low melt concentrations (<2%) in the upper mantle (above 60 km depth), presumably produced by pressure-release melting in the ridge upwelling zone.

3. A sub-crustal low-velocity lithospheric layer forms near the ridge and is present to at least ~20 Ma. Shear wave velocities within this ~7 km thick layer are intermediate between gabbro and peridotite and suggest either deep hydrothermal penetration and mantle alteration or a mantle impregnated by trapped, frozen basaltic melts. Since we find no evidence of an anomalously thick lithosphere that would be created by deep hydrothermal penetration and previous studies indicate that more melt is produced than is indicated by the thickness of the crust, we prefer the melt entrapment model. We suggest that lithospheric cooling produces a thin (5-10 km thick) lithospheric lid beneath the ridge axis that may have some effect on total melting, but also inhibits some melts from ascending out of the mantle.

TABLE 1. STARTING VELOCITY MODEL

TABLE 1. Table of values used for starting velocity model. The crustal model is based on velocities found in previous local seismic studies [*Klingelhöfer et al*., 2000]. The upper mantle model is based on the half-spaced cooling derived, frequency dependent method of *Faul and Jackson* [2005].

TABLE 1. STARTING VELOCITY MODEL

THICKNESS (km)	Vp (km/s)	Vs (km/s)	ρ (g/cm^3)
0.5	2.70	1.50	2.60
1.3	3.96	2.2	2.80
2.4	5.94	3.3	3.00
3.0	8.28	4.60	3.30
4.0	8.17	4.54	3.30
6.0	8.03	4.46	3.31
5.0	7.81	4.34	3.32
4.0	7.67	4.26	3.32
12.0	7.58	4.21	3.33
13.0	7.47	4.15	3.33
15.0	7.47	4.15	3.36
25.0	7.51	4.17	3.40
30.0	7.58	4.21	3.43
35.0	7.67	4.26	3.47
40.0	7.78	4.32	3.51
80.0	7.87	4.37	3.60
----	8.05	4.47	3.66

FIGURE 1. INHIBITED MELT PROCUCTION

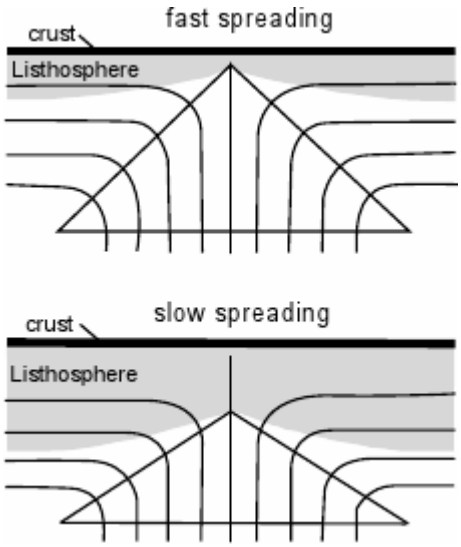

Figure 1. One theory explaining the anomalously thin crust at very slow spreading ridges suggests that mantle melting is shut off at deeper depth beneath these ridges by a thick, cold lithosphere. This thickening of the lithosphere is governed by conductive cooling of the shallow mantle in these environments. Presuming that upwelling mantle begins decompression melting at relatively the same depth beneath all ridges, a deeper shut off point reduces the overall amount of melt present in the mantle and therefore results in a thinner crust at ultra-slow spreading ridges. The area enclosed by a triangle represents the area of melting [after *Niu and Hekinian*, 1997].

FIGURE 2. THE MOHNS RIDGE AREA WITH SEISMIC EVENTS

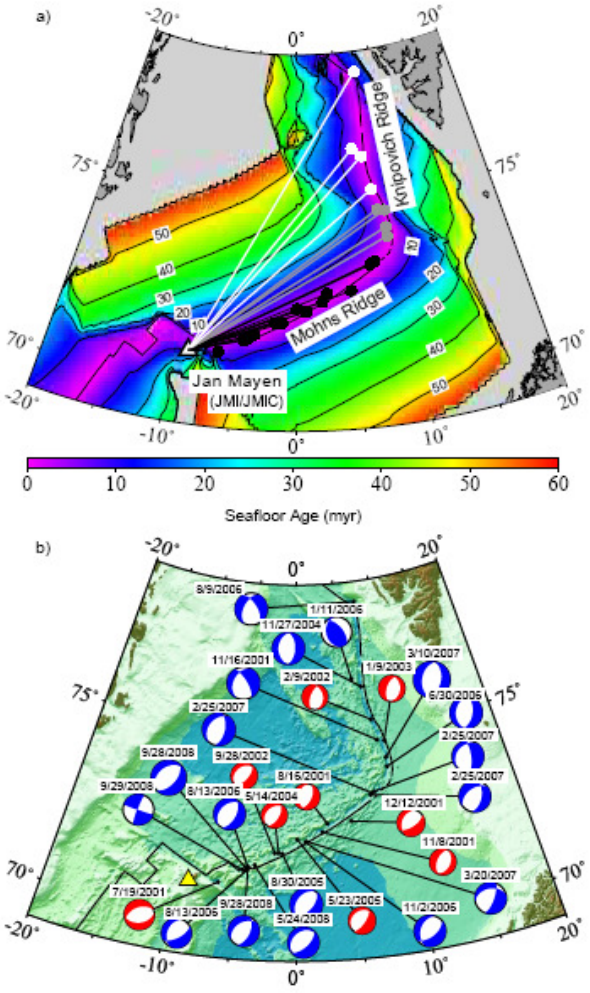

Figure 2. (a) Map depicting the age of the seafloor [*Muller et al.*, 2008] surrounding the Mohns Ridge. The ages are roughly symmetric about the ridge with the oldest seafloor dating back to approximately 60 Ma. Areas of seafloor depicted in light grey are significantly older continental shelf; darker grey areas represent neighboring land masses. The locations of seismic stations JMI and JMIC are denoted by a triangle. Earthquake epicenters are plotted as dots; the shaded lines represent great circle paths from events to stations. Black dots and lines represent events used to solve for mantle seismic structure within the lithospheric age range of 0-5 Ma, grey for 5-15 Ma, and white for 15-25 Ma. **(b)** A bathymetric map [*Jakobsson et al.*, 2008] of the Mohns Ridge region showing the 27 earthquakes employed for the analysis of the seismic structure. Focal mechanism information for each event was extracted from the International Seismological Centre *Online Bulletin* (red) (http://www.isc.ac.uk) and Global CMT Project (blue) [e.g., *Ekström et al.*, 2005] catalogs.

FIGURE 3. BROAD BAND-PASS FILTERED DATA

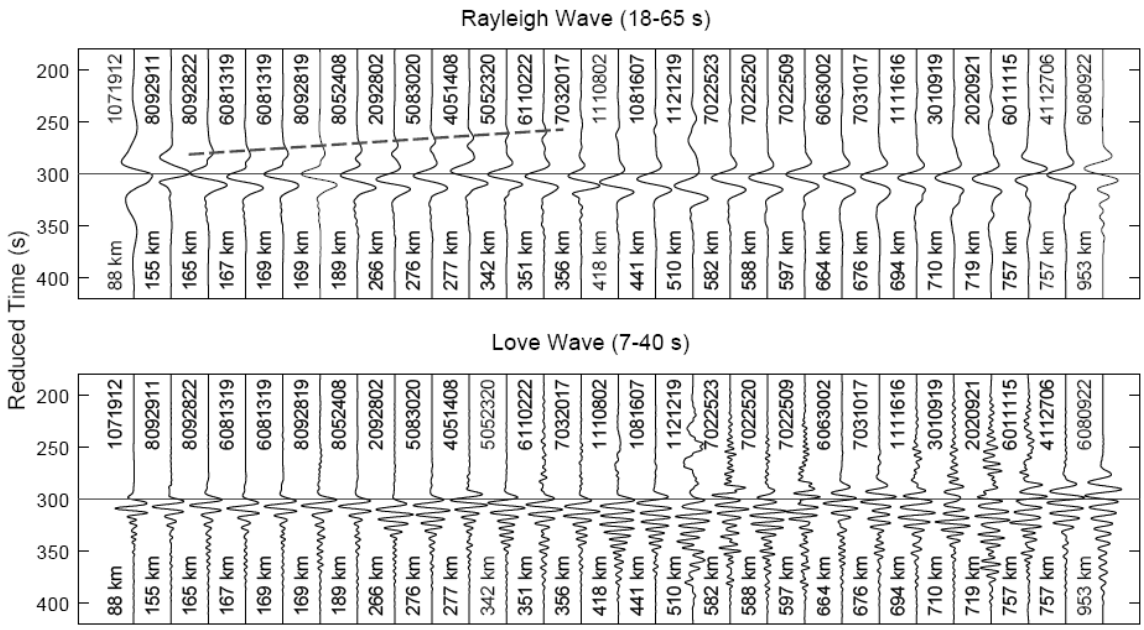

Figure 3. Plots of broad band-pass filtered data with filter corners at 18 and 65 sec for the vertical channel (top) and 7 and 40 sec for the transverse channel, (bottom). Events are ordered according to distance, as indicated on the plots. Arrival times are reduced using a velocity of 4.0 km/sec. Surface wave arrivals, as well as some body wave arrivals (for example those observed on the vertical component records ranging from ~150-350 km distance and indicated by the dashed line), are clearly observed. The relative phase shifts in waveforms for adjacent events can be attributed to the effects of variations in distance of the epicenters from the ridge axis and/or changing focal mechanisms. The data are dominated by ~30 sec (vertical channel) and ~10 sec period (transverse channel) waves.

FIGURE 4. SOLUTION - VELOCITY PROFILES

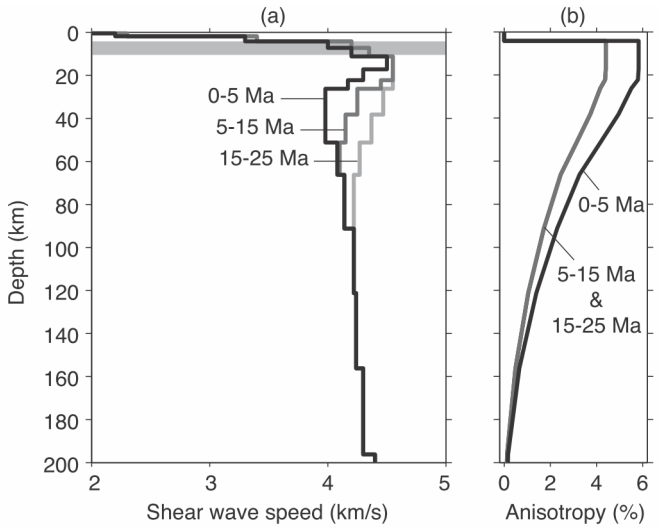

Figure 4. Solutions for the near- and off-axis **(a)** V_{SV} velocity profiles and **(b)** anisotropy profiles. In each case the vertical axis is referenced from the seafloor. Anisotropy is defined here as $(V_{SH}-V_{SV})/V_{av}$, where V_{SV} is the shear wave speed of vertically polarized waves, V_{SH} is the shear wave speed of horizontally polarized waves, and V_{av} is the average of the two. Each V_{SV} solution exhibits a ~7 km thick region of anomalously low velocities just beneath the base of the crust. This region, shaded and extending from ~4-11 km depth in the figure, has shear wave velocities intermediate between lower crustal and typical lithospheric values. The high velocity lithospheric lid is thinnest for the 0-5 Ma age range and thereafter increases with age. The 0-5 Ma profile, and to a lesser extent the 5-15 Ma profile, also exhibit a sub-lithospheric low velocity zone in the depth range of ~20-70 km that is not apparent at the oldest ages. Anisotropy, such that $V_{SH} > V_{SV}$, is detected in the upper mantle; it is strongest just beneath the crust and decays with depth. The anisotropy is generally less at older ages, but this may simply be a consequence of the different (non-ideal) azimuths of the seismic ray paths.

FIGURE 5. DATA FITS

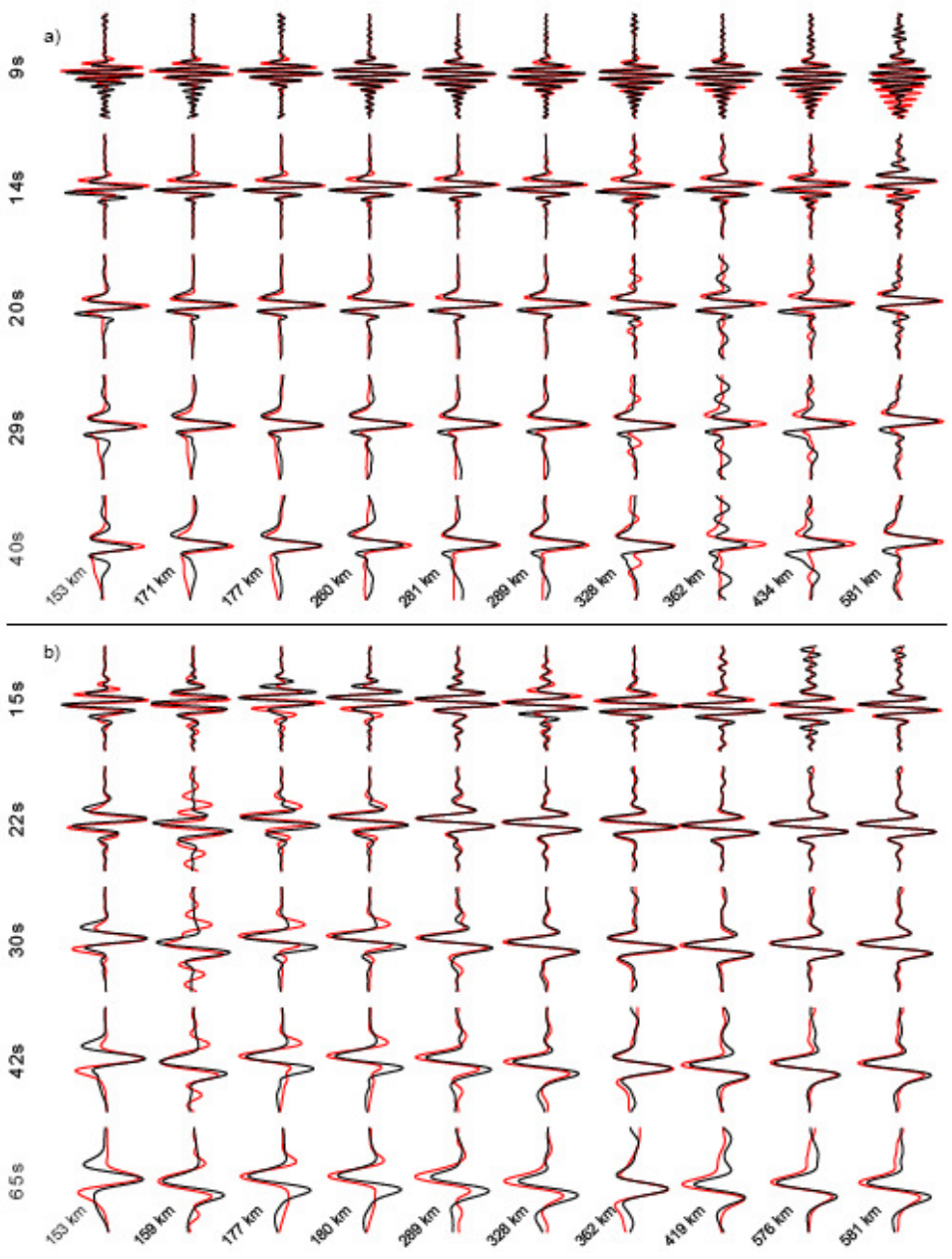

Figure 5. Observed data and corresponding synthetics for the 0-5 Ma age range for both Love **(a)** and Rayleigh **(b)** waves. The black curves are the observed data and the red curves are the synthetics. Select events are shown at several center periods (using a Gaussian-shaped band-pass filter), as indicated on the plots. Actual misfit values are given in **Figure 6b**.

FIGURE 6. SENSITIVITY TEST RESULTS

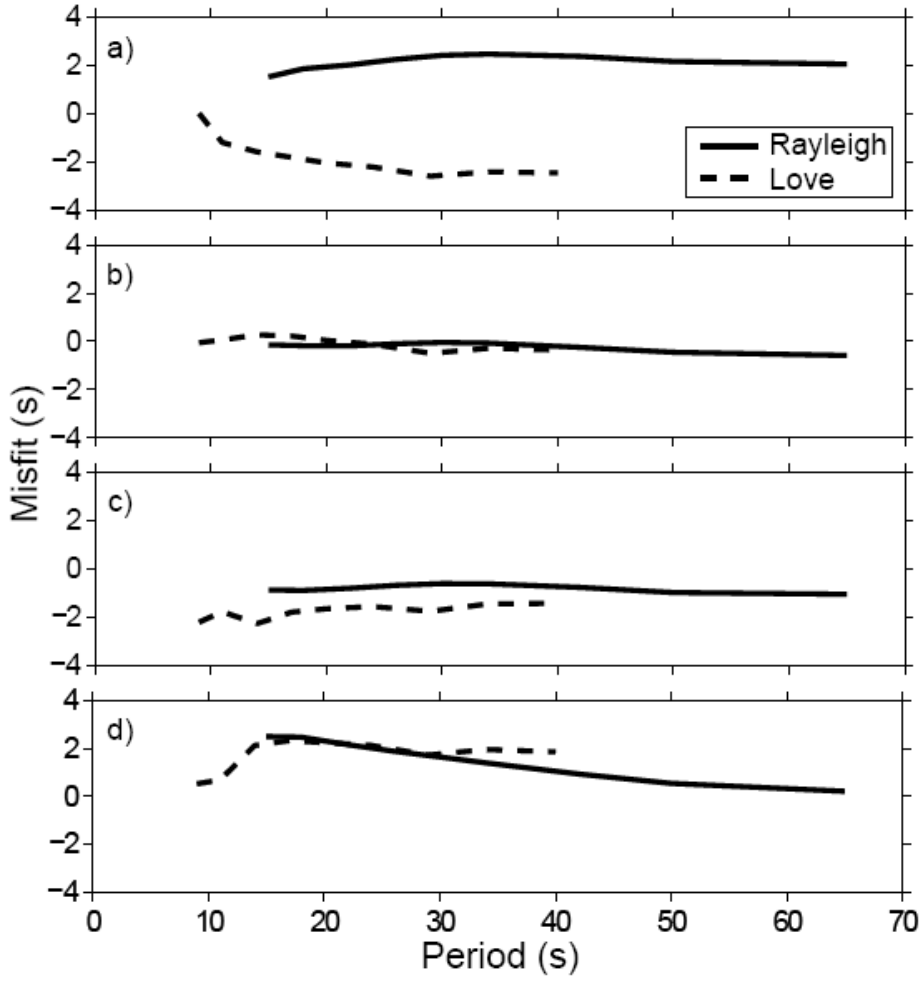

Figure 6. Plots of Rayleigh and Love misfit, calculated as the phase difference in seconds between the observed and the synthetic wavelets, as a function of period. The value plotted for each period is the average misfit for all events at that period. These plots illustrate the modeling sensitivity to small changes in shear velocity. Positive values indicate the model is too fast (early arrivals) while negative values indicate the model is too slow (late arrivals). **(a)** The misfit relative to the starting isotropic seismic model for the 0-5 Ma age range. The starting model fits the data quite well, but with an obvious Love-Rayleigh (radial anisotropy) disparity. **(b)** The misfit relative to the final anisotropic velocity model of **Figure 4**, 0-5 Ma range. The trends and means of the misfit curves of **(a)** disappear. **(c)** The final anisotropic model, 0-5 Ma, with a thicker, ~6 km, crust. **(d)** The final anisotropic model, 0-5 Ma, with an enforced 18 km thick lithosphere.

FIGURE 7. FINAL MODEL COMPARISONS

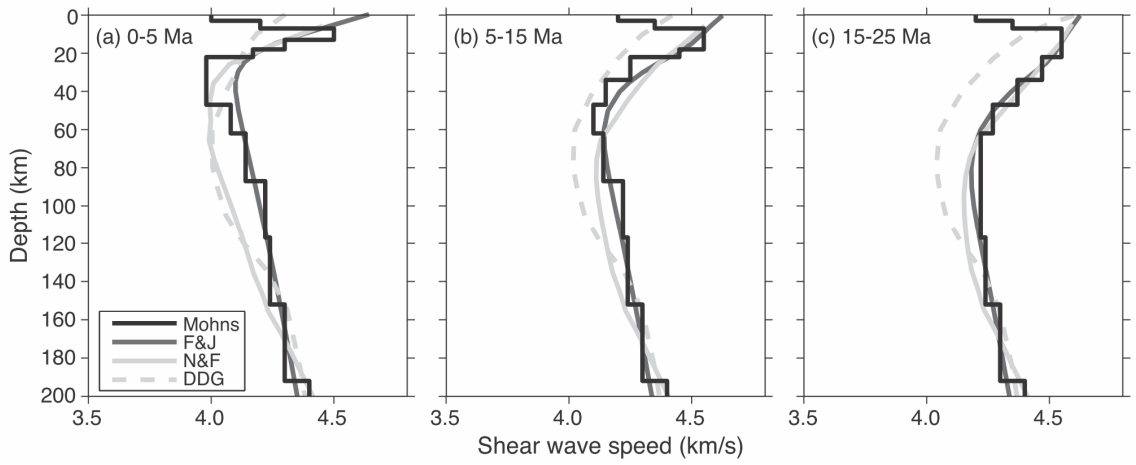

Figure 7. Mohns Ridge V_{SV} models as compared to other V_{SV} models for the same age ranges. These models include a half-space cooling model converted to seismic shear wave speed via the method of *Faul and Jackson* [2005] (F&J), the Pacific mantle model of *Nishimura and Forsyth* [1989] (N&F; their results have been interpolated to our age ranges), and the north Atlantic, Reykjanes Ridge, model of *Delorey et al.* [2007] (DDG). All models are referenced to the base of the crust in this figure. The F&J model shown here is different from that used as our starting model. Here, the F&J model has a lower reference temperature at the top of the mantle (600°C versus 650°C) and a smaller grain size (2 mm versus 5 mm) that results in an overall better correlation with the Mohns Ridge models. The greatest variation between the four models occurs within the 0-5 Ma age range where each of the data-derived models has lower sub-lithospheric shear velocities than the F&J model, which is derived from temperature and pressure effects on mantle materials. Such a deviation may indicate the presence of a small amount of melt in the upper mantle. Only the Mohns model contains the sub-crustal low velocity (ALVIN) region in the topmost ~7 km of the mantle.

FIGURE 8. CARTOON - PREFERRED MODEL

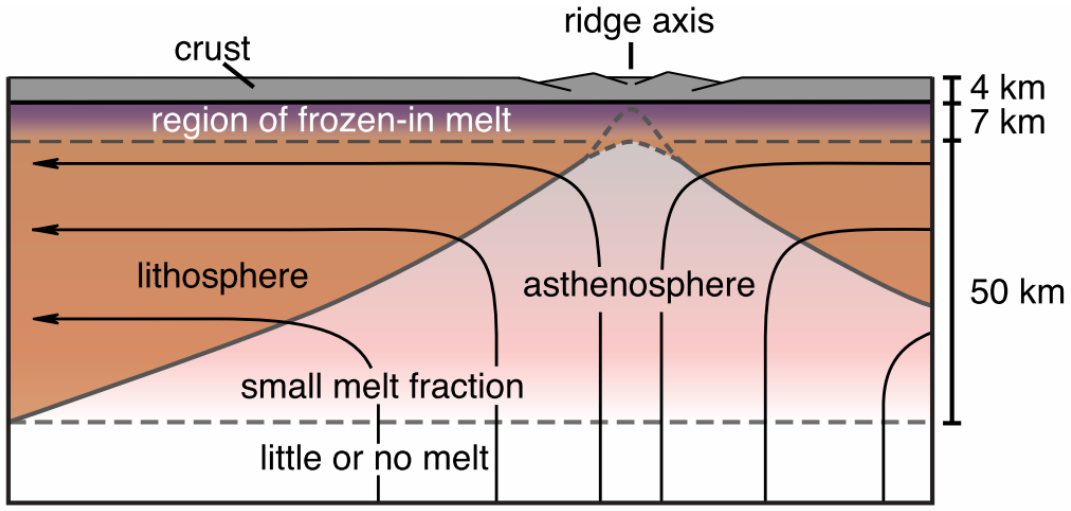

Figure 8. Cartoon depicting our preferred interpretation of the Mohns Ridge mantle seismic structure. Lines with arrows indicate mantle flow lines. A slightly thickened axial lithosphere inhibits the migration of melt towards the surface. As a result, melt freezes into the top ~7 km of the mantle resulting in shear wave speeds that are intermediate between crustal and mantle values. The cartoon depicts little to no melt below ~60 km depth below the crust as is suggested by comparing the Mohns Ridge seismic results to the F&J temperature-only model in **Figure 7**. However, it is possible to make various shear wave predictions using the *Faul and Jackson* [2005] method and the possibility of trace amounts of melt below 60 km depth cannot be ruled out.

APPENDIX A. EVENT PARAMETERS

Event parameters are obtained from the Global Centroid Moment Tensor Project **(Table A-1)** and the International Seismological Centre **(Table A-2)** for the area 70° to 82° N, -28° to 17° E. Event parameters include date, time, location, magnitude, moment tensor, and best double couple. Moment tensor information is reported in standard spherical notation with the reference frame $r = up$, $\theta = south$, and $\varphi = east$, and is converted to Cartesian notation with the *Aki and Richards* [2002] convention of $x = north$, $y = east$, and $z = down$ with the following relation:

$$M = \begin{pmatrix} M_{rr} & M_{r\theta} & M_{r\phi} \\ M_{\theta r} & M_{\theta\theta} & M_{\theta\phi} \\ M_{\phi r} & M_{\phi\theta} & M_{\phi\phi} \end{pmatrix} = \begin{pmatrix} M_{zz} & M_{zx} & -M_{zy} \\ M_{xz} & M_{xx} & -M_{xy} \\ -M_{yz} & -M_{yx} & M_{yy} \end{pmatrix}.$$

The moment tensor contains information about the fault geometry of the event and the event size. The best double couple, a mapping of the moment tensor to the best-fit planar fault geometry, contains information about the fault geometry only. Either moment tensor or best double couple information can be used to forward model seismic waves [*Stein and Wysession*, 2003].

APPENDIX B. EARTHQUAKE RADIATION PATTERNS

To accurately forward model seismic waves for comparison to the recorded data, the radiation pattern of the earthquake must be calculated. This can be done using either the event moment tensor or the event best double couple. Both the moment tensor and the best double couple describe the event fault geometry, and, as such, contain information about the initial phase and radiation pattern of the seismic waves [*Stein and Wysession*, 2003]. In terms of the event moment tensor, radiation patterns are calculated using equations *58* and *59* from *Yomogida and Aki* [1985] for Love and Rayleigh waves respectively. Because the best double couple is a simplified description of an earthquake's fault geometry and is typically as accurate as the moment tensor (since non-double couple components tend to be small), the best double couple will be used to calculate radiation patterns.

Love and Rayleigh wave radiation pattern information for each event obtained from the Global CMT and ISC catalogs is given in **Figures B1-27**. The top and bottom portion of each section contains plots of the initial phase and amplitude of the seismic wave respectively. All plots are a function of period. Periods range from 65s to 8s for Love waves and 65s to 15s for Rayleigh waves. Straight lines indicate great circle path from event epicenter to seismic station location. Only events with relatively constant phase and amplitude in the direction of the station were retained for analysis.

APPENDIX C. PRELIMINARY DATA PROCESSING AND ANALYSIS

Raw gse-format data are obtained from the NORSAR website via AutoDRM request. Upon acquisition, raw data in GSE2.0 format are first converted to sac-format using seismic analysis code, SAC2000 [*Goldstein*, 1996]. Because SAC2000 is designed specifically for the analysis of seismic data, SAC2000 is predominantly used for data processing and preliminary analysis.

During the conversion from gse- to sac-format data, SAC2000 automatically produces three separate files, vertical, north, and east, corresponding to each of the three components of the Streckeisen STS-2 seismometer. Although north and east are standard conventions for the alignment of the horizontal components, extensive teleseismic testing determined that station JMI was incorrectly recorded with east-west and north-south components being swapped. Jens Havskov of the University of Bergen (Norway) confirmed a problem with station JMI for the time period of April 2000 to October 2001. All events during this period are corrected to attain consistency between data sets. Additional numerical testing determined station JMI to be misaligned by approximately -16° from north as shown in **Figure C-1**. All JMI data are further corrected for this error. After all corrections, the horizontals are rotated to recover the radial and transverse components of the data.

To avoid inducing aliasing and leakage to the data, the data are detrended, and then tapered using a symmetric 20% Hanning taper. Instrument response is removed using SAC2000 and the poles and zeros values listed in **Table D-2** for each respective station. The process of removing the instrument response is described in further detail in **Appendix D**. Predicted arrival times for the compressional P-wave and shear S-wave are determined using the travel time program TAUP. Predicted arrival times are based upon the IASPEI91 global velocity model. The data are further filtered using a Gaussian filter to examine data at narrow frequency bands. Center frequencies of the Gaussian filter range from 0.1 to 1.0 Hz. Filtered data are windowed around P- and S-wave arrivals and again tapered using a symmetric Hanning taper of 10%. To extract group velocities, the envelope of the windowed data is determined using the SAC2000 *envelope* command. Taking the cross-correlation of the seismic data is a type of preliminary analysis allowing

a visual observation of variable seismic velocity along the ridge. As such, data are cross-correlated in Matlab to observe relative group travel time delays **(Figure C-2)**. Windowed component data are plotted against each other to produce particle motion plots **(Figure C-3)**. Plots are positioned as a function of distance from the station along the ridge. An extreme shift in polarization of adjacent particle motion plots first indicated the misalignment of one of the seismic stations. To gain insight into the frequency content of the data, both raw data and filtered data are plotted with their associated frequency spectrum **(Figure C-4)**. Raw data are characterized by microseismic noise ~0.1-0.3 Hz, which is eliminated by filtering.

APPENDIX D. INSTRUMENT PARAMETERS AND RESPONSES

Broadband stations JMI and JMIC are both Streckeisen STS-2 instruments owned and operated by Norwegian research groups, JMI by NNSN and JMIC by NORSAR. Instrument response files for stations JMI and JMIC were provided by NNSN. The response file for station JMI contains only the nominal response which matches the general manufacturer's response for an STS-2 instrument as provided by IRIS (http://www.iris.edu/hq/programs/passcal/instrumentation) while the JMIC file contains the full response and is unique to station JMIC. **Tables D-1** and **D-2** list instrument locations and specific properties for both stations as well as general information for the STS-2 model. A plot of the instrument response for the STS-2 as provided by the manufacturer is shown in **Figures D-1**. **Figure D-2** shows the unique instrument responses for stations JMI and JMIC as compared to the nominal response provided by the manufacturer.

Before a record of true ground motion is obtained from the raw seismic data, the instrument response is removed. Raw data are recorded in units of volts/nm and are distributed as such. Therefore, data must be used in conjunction with a poles and zeros file which numerically expresses the instrument response. Mathematically, the instrument response is described by the equation

$$V(\omega) = A_i \frac{\Pi_{j=1}^{k}(i\omega - z_j)}{\Pi_{j=1}^{m}(i\omega - p_j)}$$

where ω is the angular frequency, A_i is the scaling factor of the instrument response, and the poles (p_j) and zeros (z_j) are the roots of the denominator and numerator polynomials, respectively [*Scherbaum*, 2001; *Nolet*, 2008]. Seismic analysis code SAC2000, [*Goldstein*, 1996] designed specifically for the analysis of seismic data, is equipped with a transfer command that performs a deconvolution based on the poles and zeros information to remove the instrument response. Once the deconvolution is complete, a record of true ground motion is obtained.

APPENDIX E. FORWARD MODELING WAVEFORMS

The subroutine to calculate synthetic seismograms is based on original reflectivity method of *Randall* [1994] as modified by *Xu and Weins* [1997] to add a water layer. Primary inputs include earthquake parameters, starting velocity model, and range of frequencies and slownesses to integrate over. The subroutine also incorporates an overlying water layer. The subroutine returns synthetic waveforms on the vertical, radial, and transverse components.

To verify the code, results were compared to an exact 2D response of an explosional force in an elastic halfspace with a free surface (Garvin's Problem). Code for the exact response (EX2DVAEL) was obtained from the ***S***eismic Wave ***P***ropagation and ***I***maging in ***C***omplex Media: A ***E***uropean Network (SPICE) website (http://www.spice-rtn.org/home). To ensure common frequency content between the two data sets, the amplitude spectrum input into the Randall code was matched to the amplitude spectrum of the SPICE code. Results are shown in **Figure E**. The excellent agreement between the two data sets suggests that the results of the Randall code are reliable.

APPENDIX F. EVENT RELOCATIONS

Epicenter location errors are removed for each event using a grid search method over the event-to-station range. The range varied from -26km (closer to the station) to +26km (further from the station) in 0.1km intervals while always maintaining a constant azimuth. The grid search is performed using the five longest periods of the data (30s, 34s, 42s, 50s, and 65s for the Rayleigh waves and 14s, 18s, 24s, 29s, and 40s for the Love waves) to better constrain the actual event epicenter. Waveform misfits for each period are converted to a probability distribution and the joint probability distribution is calculated as the product of the individual distributions. The mean change in range is removed from the relocation of each event to account for any bias in the relocation caused by any inaccuracies in the velocity model used when calculating the synthetic data. **Table F** lists each event along with the de-meaned change in range and before and after misfit values for the 26s, 34s, and 50s data. **Figure F** shows a comparison of the vertical component of the recorded data, the vertical component of the synthetic waveform created at the original epicenter, and the vertical component of the synthetic waveform created at the relocated epicenter.

TABLE A-1. CMT EVENT PARAMETERS

TABLE A-1. Earthquakes recorded by stations JMI and JMIC. Data are from the Global CMT Project (www.globalcmt.org).

TABLE A-1. CMT EVENT DATE, TIME, LOCATION AND MAGNITUDE.

EVENT	DATE	TIME	LAT	LON	DEPTH	Ms	Mw
111601E	2001/11/16	16:19:40	74.72	8.08	15.0	4.8	5.1
112704B	2004/11/27	06:38:29	76.18	7.16	12.0	4.5	5.1
200508302053A	2005/08/30	20:53:50	71.84	-1.23	12.0	4.5	5.0
200601111513A	2006/01/11	15:13:44	76.41	6.20	15.8	4.0	4.8
200606300243A	2006/06/30	02:43:35	73.98	8.68	12.0	4.0	5.1
200608092231A	2006/08/09	22:31:14	78.46	7.64	12.0	4.2	5.1
200608131903A	2006/08/13	19:03:08	71.45	-4.05	12.0	4.1	5.0
200608131943A	2006/08/13	19:43:08	71.38	-4.06	12.0	--	4.7
200611022252A	2006/11/02	22:52:41	72.14	0.75	12.0	--	4.9
200702250913A	2007/02/25	09:13:54	73.37	7.21	12.0	--	4.9
200702252013A	2007/02/25	20:13:45	73.33	6.96	12.0	4.4	5.1
200702252312A	2007/02/25	23:12:27	73.29	6.80	12.0	--	4.9
200703101703A	2007/03/10	17:03:39	74.23	8.72	12.0	5.7	5.7
200703201703A	2007/03/20	17:03:39	72.16	0.86	12.0	4.0	4.9
200805240818A	2008/05/24	08:18:17	71.51	-3.50	12.0	--	4.9
200809281952A	2008/09/28	19:52:24	71.44	-4.03	12.0	--	4.8
200809282220A	2008/09/28	22:20:21	71.39	-4.11	12.0	5.5	5.5
200809291103A	2008/09/29	11:03:56	71.34	-4.35	12.0	4.0	4.8

TABLE A-1 (cont.). MOMENT TENSOR

EVENT (ABR)	Exp	Mxx/ error	Myy/ error	Mzz/ error	Mxy/ error	Myz/ error	Mxz/ error
111601E	23	-0.30 0.5	3.74 0.3	-3.44 0.3	-1.04 0.3	2.52 1.7	3.38 1.3
112704B	23	-0.13 0.1	4.81 0.1	-4.67 0.1	-0.79 0.1	1.48 0.3	-0.29 0.4
50830A	23	1.76 0.1	2.82 0.1	-4.58 0.1	-1.97 0.1	1.03 0.3	-1.18 0.4
60111A	23	-0.08 0.1	-1.61 0.1	1.69 0.1	-0.68 0.1	-0.59 0.2	-0.69 0.3
60630A	23	-0.04 0.1	4.41 0.1	-4.37 0.1	-1.36 0.1	1.66 0.3	-0.55 0.4
60809A	23	-2.61 0.1	5.88 0.1	-3.28 0.1	-0.64 0.1	0.79 0.3	0.81 0.4
60813A	23	0.83 0.1	2.23 0.1	-3.06 0.1	-1.56 0.1	1.16 0.2	-0.17 0.3
60813A	23	0.36 0.1	0.66 0.1	-1.04 0.1	-0.54 0.1	0.05 0.3	-0.68 0.4
61102A	23	0.89 0.1	1.87 0.1	-2.77 0.1	-1.13 0.1	0.23 0.4	-1.52 0.5
70225A	23	0.79 0.1	1.31 0.1	-2.11 0.1	-0.85 0.1	2.47 0.3	0.74 0.3
70225A	23	1.78 0.1	3.84 0.1	-5.62 0.1	-2.45 0.1	2.86 0.4	0.18 0.5
70225A	23	1.06 0.1	1.60 0.1	-2.67 0.1	-1.36 0.1	1.09 0.3	0.85 0.4
70310A	24	0.21 0.0	4.04 0.0	-4.25 0.0	-1.50 0.0	0.16 0.1	-0.14 0.1
70320A	23	0.97 0.1	0.59 0.1	-1.57 0.1	-2.02 0.1	1.83 0.3	-0.54 0.3
80524A	23	1.11 0.1	1.14 0.1	-2.25 0.1	-1.13 0.1	1.14 0.3	-1.03 0.3
80928A	23	0.73 0.1	1.19 0.1	-1.93 0.1	-0.86 0.1	0.84 0.2	0.28 0.3
80928A	24	0.90 0.0	1.10 0.0	-2.01 0.0	-1.07 0.0	0.57 0.1	-0.30 0.1
80929A	23	1.71 0.1	-0.59 0.1	-1.12 0.1	-1.82 0.1	0.01 0.2	-0.12 0.2

TABLE A-1 (cont.). BEST DOUBLE COUPLE

EVENT	STRIKE 1	DIP 1	SLIP 1	STRIKE 2	DIP 2	SLIP 2
111601E	216	37	-37	337	69	-121
112704B	188	36	-91	10	54	-89
200508302053A	214	36	-96	41	55	-86
200601111513A	173	34	113	326	59	75
200606300243A	194	35	-92	17	55	-89
200608092231A	215	50	-43	336	58	-131
200608131903A	222	36	-76	24	55	-100
200608131943A	198	36	-125	59	61	-67
200611022252A	198	37	-119	52	58	-70
200702250913A	228	26	-45	0	72	-109
200702252013A	227	35	-66	19	58	-106
200702252312A	240	46	-57	17	53	-119
200703101703A	198	44	-92	20	46	-88
200703201703A	261	37	-35	20	70	-122
200805240818A	226	28	-87	43	62	-91
200809281952A	234	40	-63	20	55	-111
200809282220A	227	37	-83	38	54	-95
200809291103A	196	84	-177	106	87	-6

TABLE A-2. ISC EVENT PARAMETERS

TABLE A-2. Earthquakes recorded by stations JMI and JMIC. Data are from the International Seismological Centre (http://www.isc.ac.uk/) as reported to ISC by the Swiss Seismological Service (http://www.seismo.ethz.ch/).

TABLE A-2. ISC EVENT DATE, TIME, LOCATION AND MAGNITUDE

EVENT	DATE	TIME	LAT	LON	DEPTH	IDC MS
1954476	2001/07/19	12:01:34	70.9790	-6.3380	9.0	4.7
2051704	2001/08/16	07:08:22	72.6180	2.7070	9.0	4.1
2331828	2001/11/08	02:00:05	72.3950	2.2360	4.0	4.1
2429100	2001/12/12	19:44:17	72.6460	4.8350	6.0	4.3
2891473	2002/02/09	21:48:04	75.2770	7.7910	6.0	4.0
3443452	2002/09/28	02:36:37	71.8470	-1.8470	12.0	4.1
6533903	2003/01/09	19:29:22	74.6800	8.7970	6.0	4.1
7342970	2004/05/14	08:28:59	71.8490	-1.5230	9.0	4.0
7382123	2005/05/23	20:18:27	72.2180	0.0510	4.0	4.2

TABLE A-2 (CONT.). MOMENT TENSOR

EVENT	Mxx	Myy	Mzz	Mxy	Myz	Mxz
1954476	2.120	0.088	-2.208	-0.835	-0.256	0.025
2051704	0.714	2.145	-2.858	-0.451	0.671	-0.799
2331828	0.358	1.047	-1.405	-0.420	-0.282	0.079
2429100	1.131	1.483	-2.614	-0.780	0.072	-1.698
2891473	0.265	1.102	-1.367	-0.131	-0.447	0.606
3443452	0.964	1.011	-1.975	-0.778	0.949	-0.611
6533903	0.471	1.695	-2.166	-0.478	-0.615	0.515
7342970	0.605	0.780	-1.385	-0.491	0.581	-0.107
7382123	0.742	0.755	-1.497	-0.747	1.299	-0.740

TABLE A-2 (CONT.). BEST DOUBLE COUPLE

EVENT	STRIKE 1	DIP1	SLIP 1	STRIKE 2	DIP 2	SLIP 2
1954476	244.00	47.00	-99.00	77.00	44.00	-81.00
2051704	26.00	55.00	-80.00	189.00	36.00	-104.00
2331828	203.00	51.00	-92.00	27.00	39.00	-87.00
2429100	62.00	62.00	-72.00	208.00	33.00	-119.00
2891473	207.00	59.00	-74.00	358.00	34.00	-115.00
3443452	39.00	61.00	-95.00	228.00	30.00	-81.00
6533903	206.00	56.00	-83.00	14.00	35.00	-100.00
7342970	29.00	57.00	-100.00	228.00	35.00	-75.00
7382123	34.00	68.00	-98.00	234.00	24.00	-71.00

FIGURE B-1. RADIATION PATTERNS

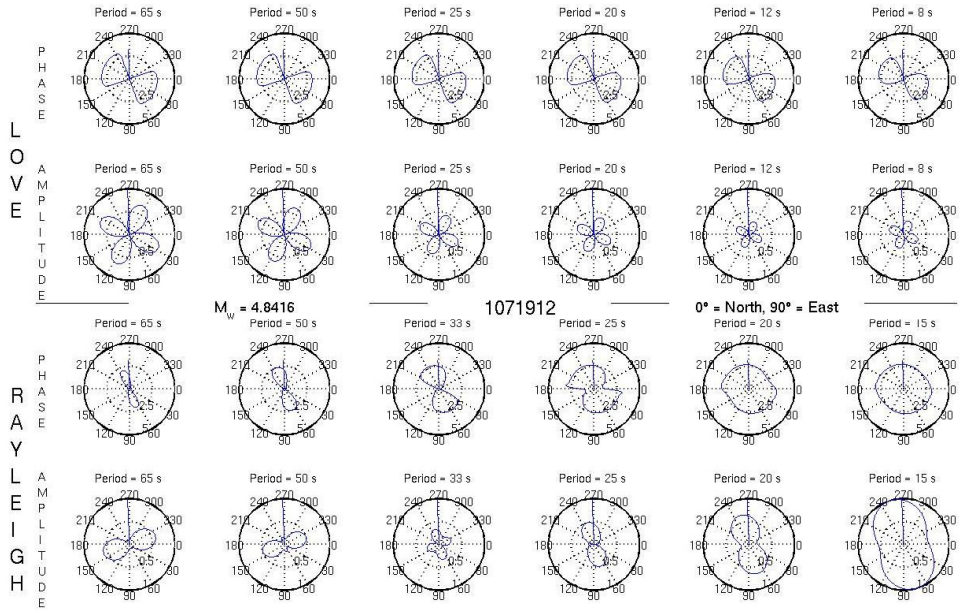

Figure B-1. Love (top) and Rayleigh (bottom) wave radiation pattern for event 1071912. The top and bottom portion of each section contains plots of the initial phase and amplitude of the seismic wave respectively. All plots are a function of period. Straight lines indicate great circle path from event epicenter to seismic station location.

FIGURE B-2. RADIATION PATTERNS

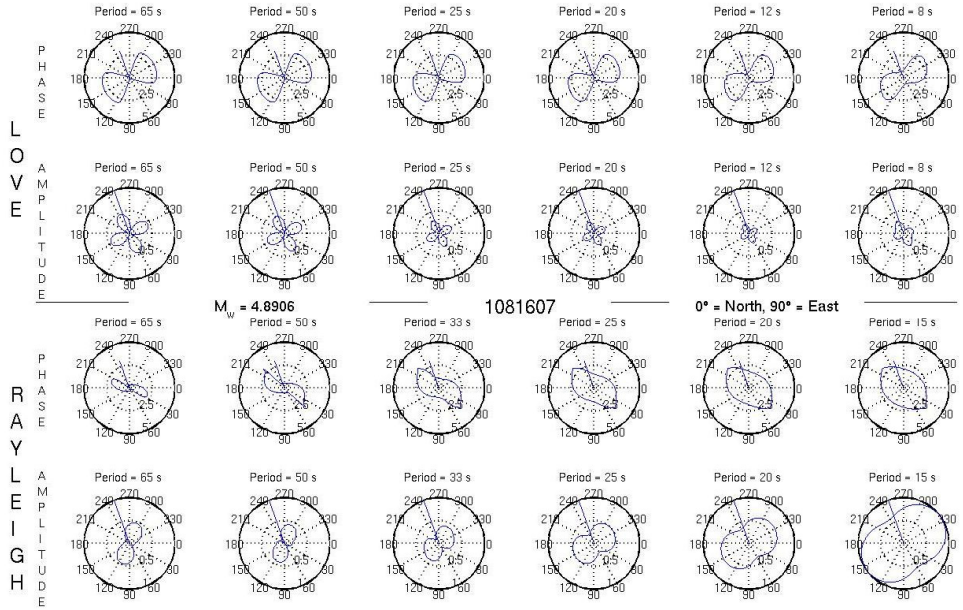

Figure B-2. Love (top) and Rayleigh (bottom) wave radiation pattern for event 1081607. The top and bottom portion of each section contains plots of the initial phase and amplitude of the seismic wave respectively. All plots are a function of period. Straight lines indicate great circle path from event epicenter to seismic station location.

FIGURE B-3. RADIATION PATTERNS

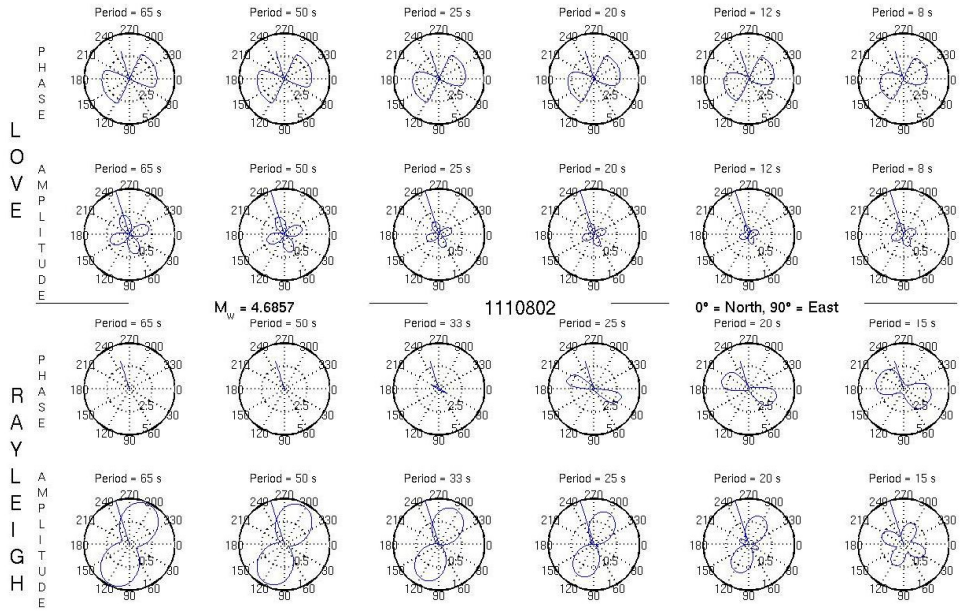

Figure B-3. Love (top) and Rayleigh (bottom) wave radiation pattern for event 1110802. The top and bottom portion of each section contains plots of the initial phase and amplitude of the seismic wave respectively. All plots are a function of period. Straight lines indicate great circle path from event epicenter to seismic station location.

FIGURE B-4. RADIATION PATTERNS

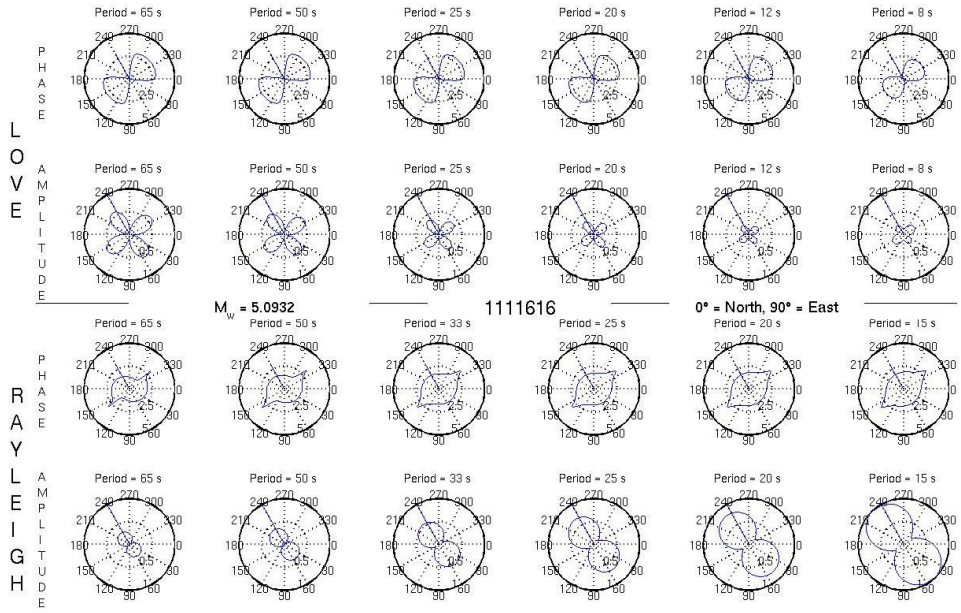

Figure B-4. Love (top) and Rayleigh (bottom) wave radiation pattern for event 1111616. The top and bottom portion of each section contains plots of the initial phase and amplitude of the seismic wave respectively. All plots are a function of period. Straight lines indicate great circle path from event epicenter to seismic station location.

FIGURE B-5. RADIATION PATTERNS

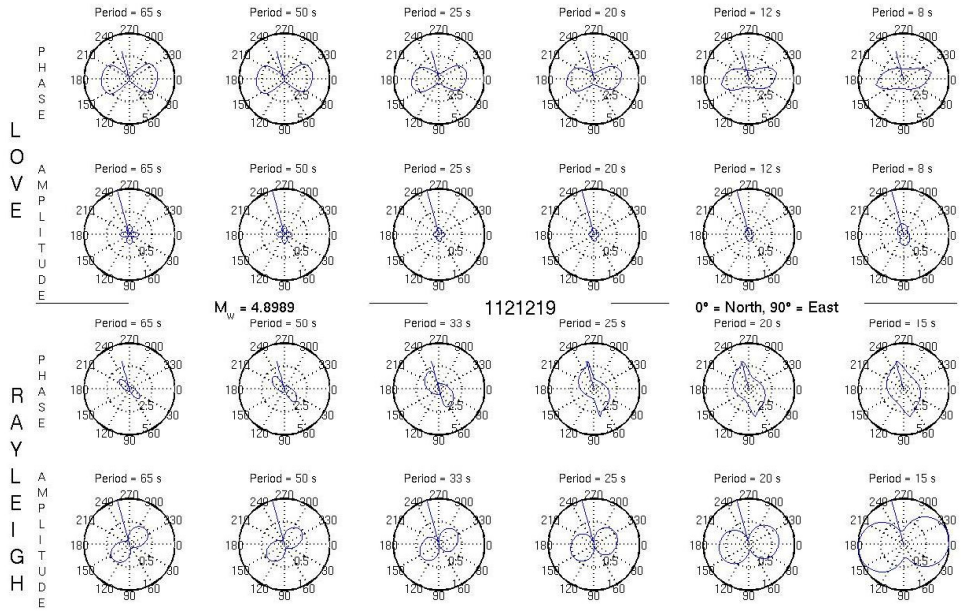

Figure B-5. Love (top) and Rayleigh (bottom) wave radiation pattern for event 1121219. The top and bottom portion of each section contains plots of the initial phase and amplitude of the seismic wave respectively. All plots are a function of period. Straight lines indicate great circle path from event epicenter to seismic station location.

FIGURE B-6. RADIATION PATTERNS

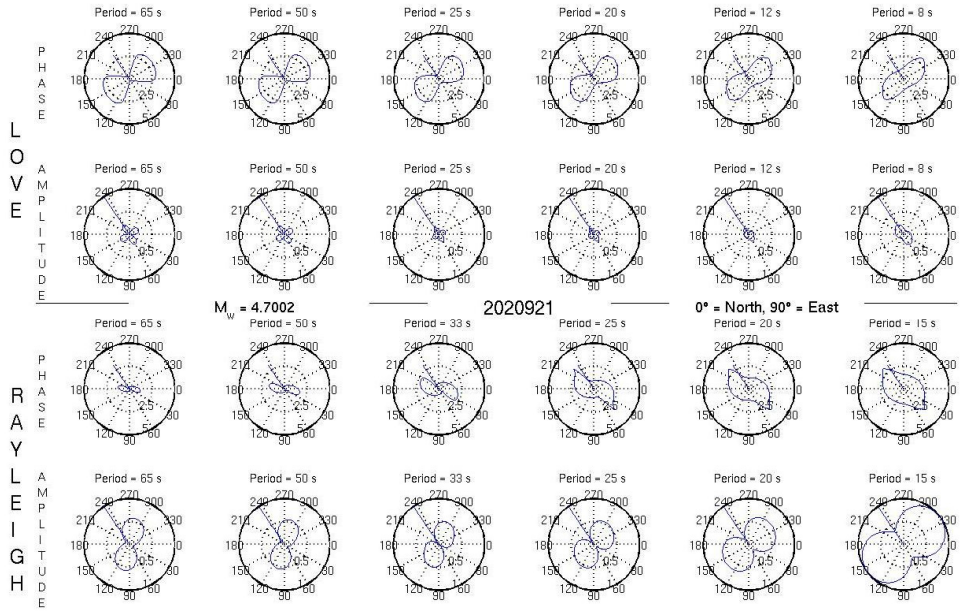

Figure B-6. Love (top) and Rayleigh (bottom) wave radiation pattern for event 2020921. The top and bottom portion of each section contains plots of the initial phase and amplitude of the seismic wave respectively. All plots are a function of period. Straight lines indicate great circle path from event epicenter to seismic station location.

FIGURE B-7. RADIATION PATTERNS

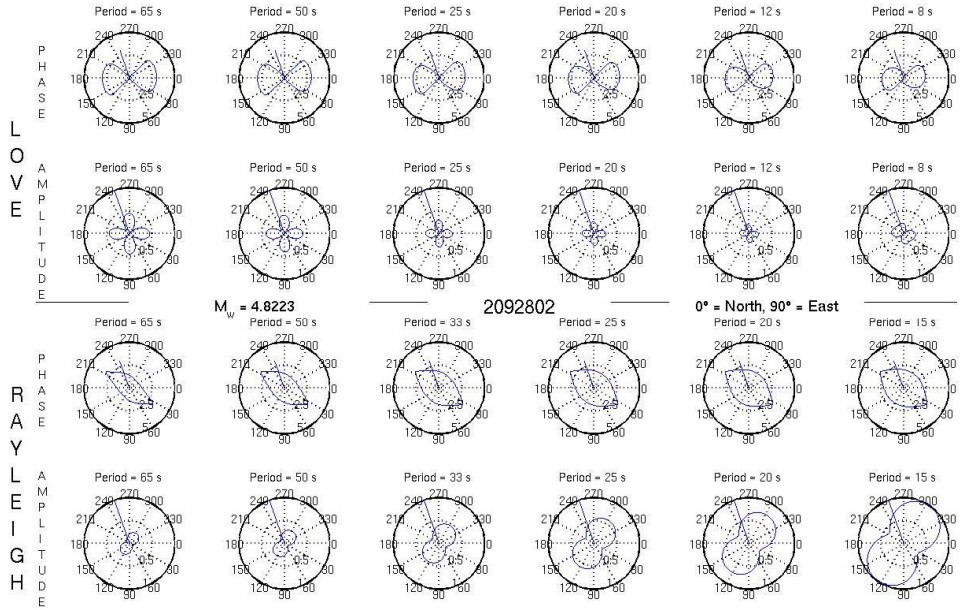

Figure B-7. Love (top) and Rayleigh (bottom) wave radiation pattern for event 2092802. The top and bottom portion of each section contains plots of the initial phase and amplitude of the seismic wave respectively. All plots are a function of period. Straight lines indicate great circle path from event epicenter to seismic station location.

FIGURE B-8. RADIATION PATTERNS

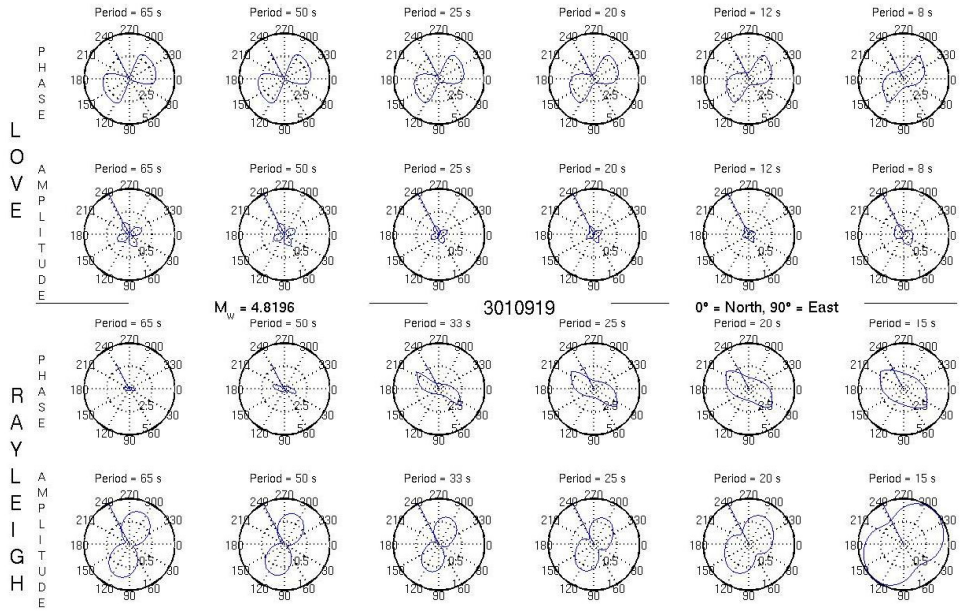

Figure B-8. Love (top) and Rayleigh (bottom) wave radiation pattern for event 3010919. The top and bottom portion of each section contains plots of the initial phase and amplitude of the seismic wave respectively. All plots are a function of period. Straight lines indicate great circle path from event epicenter to seismic station location.

FIGURE B-9. RADIATION PATTERNS

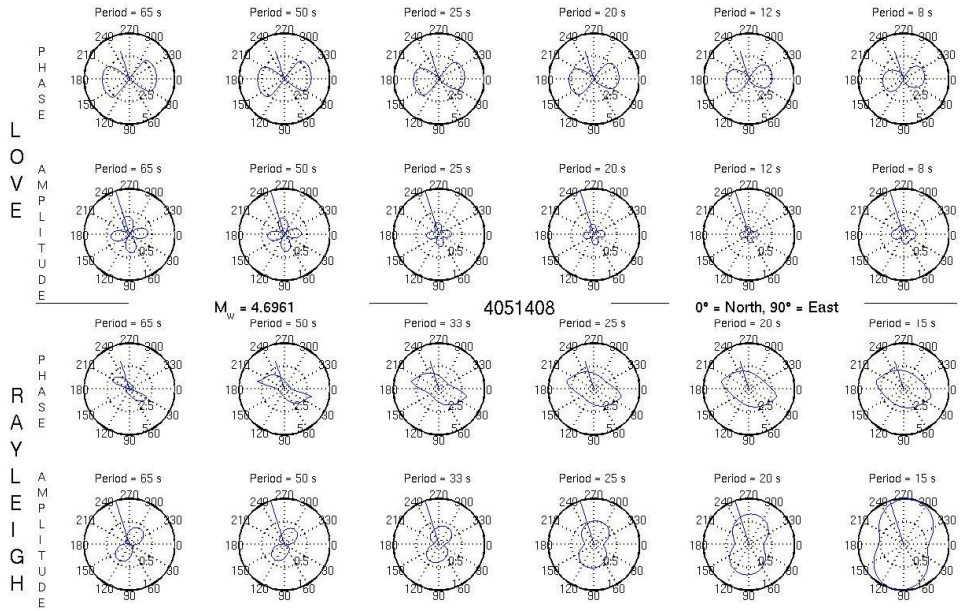

Figure B-9. Love (top) and Rayleigh (bottom) wave radiation pattern for event 4051408. The top and bottom portion of each section contains plots of the initial phase and amplitude of the seismic wave respectively. All plots are a function of period. Straight lines indicate great circle path from event epicenter to seismic station location.

FIGURE B-10. RADIATION PATTERNS

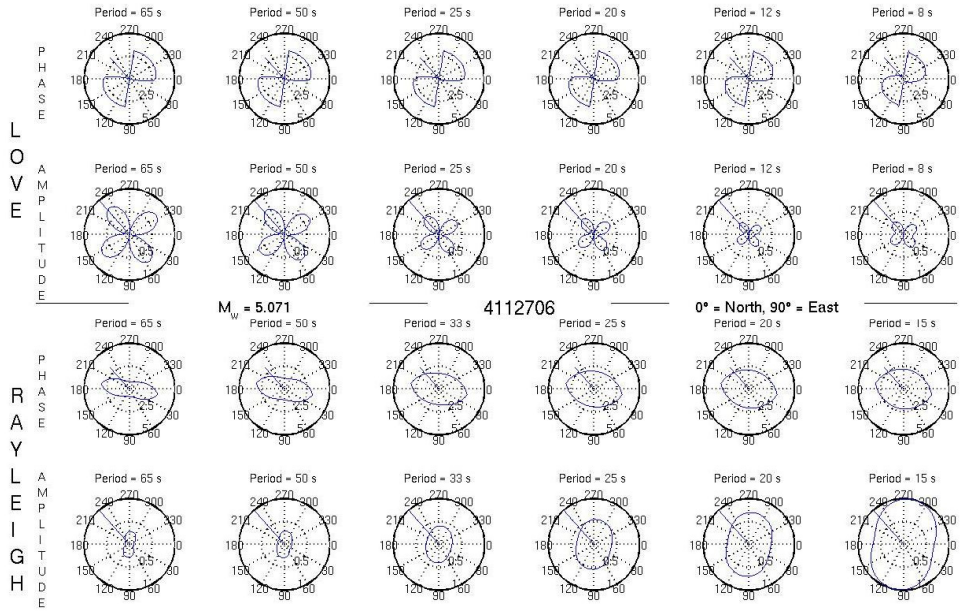

Figure B-10. Love (top) and Rayleigh (bottom) wave radiation pattern for event 4112706. The top and bottom portion of each section contains plots of the initial phase and amplitude of the seismic wave respectively. All plots are a function of period. Straight lines indicate great circle path from event epicenter to seismic station location.

FIGURE B-11. RADIATION PATTERNS

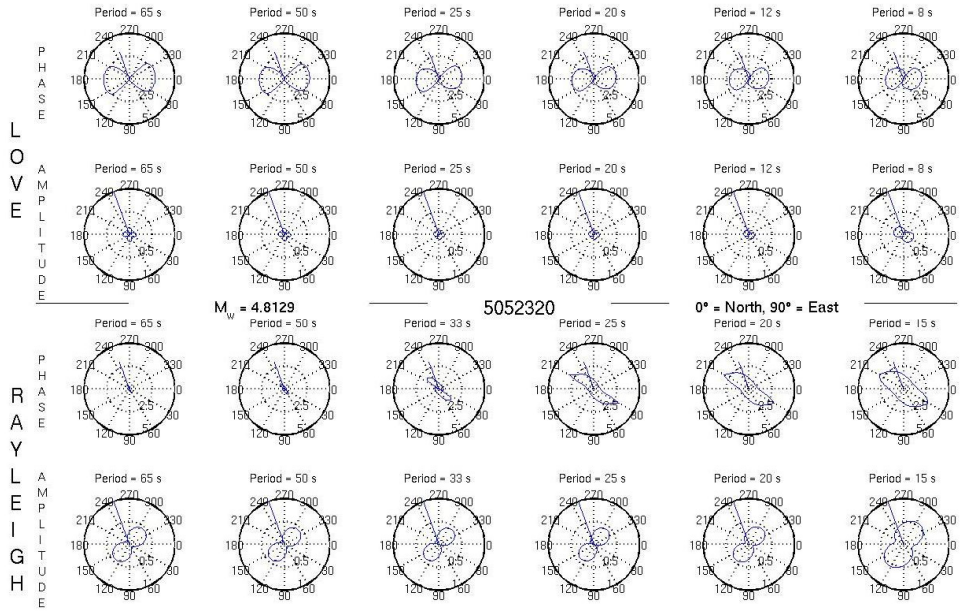

Figure B-11. Love (top) and Rayleigh (bottom) wave radiation pattern for event 5052320. The top and bottom portion of each section contains plots of the initial phase and amplitude of the seismic wave respectively. All plots are a function of period. Straight lines indicate great circle path from event epicenter to seismic station location.

FIGURE B-12. RADIATION PATTERNS

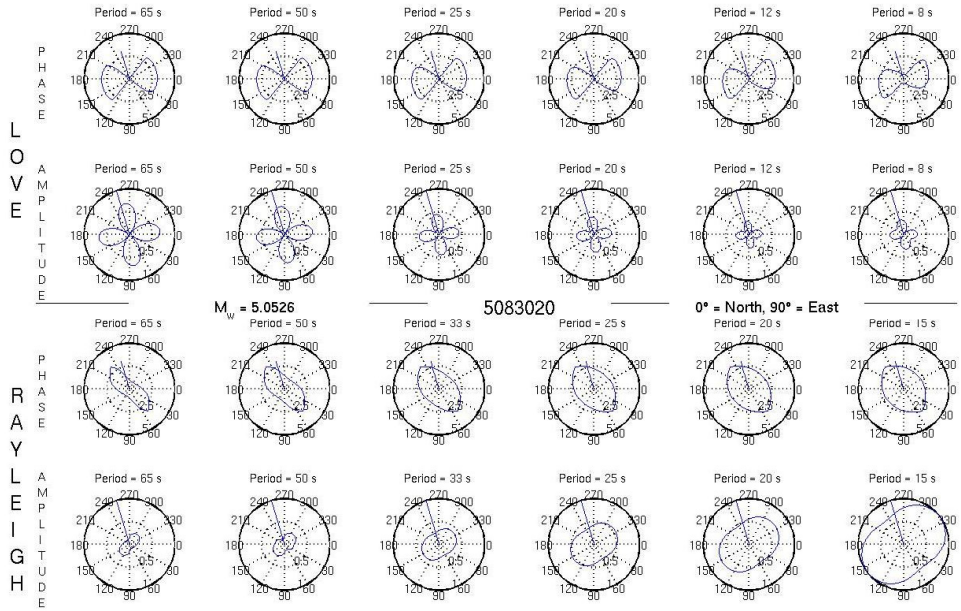

Figure B-12. Love (top) and Rayleigh (bottom) wave radiation pattern for event 5083020. The top and bottom portion of each section contains plots of the initial phase and amplitude of the seismic wave respectively. All plots are a function of period. Straight lines indicate great circle path from event epicenter to seismic station location.

FIGURE B-13. RADIATION PATTERNS

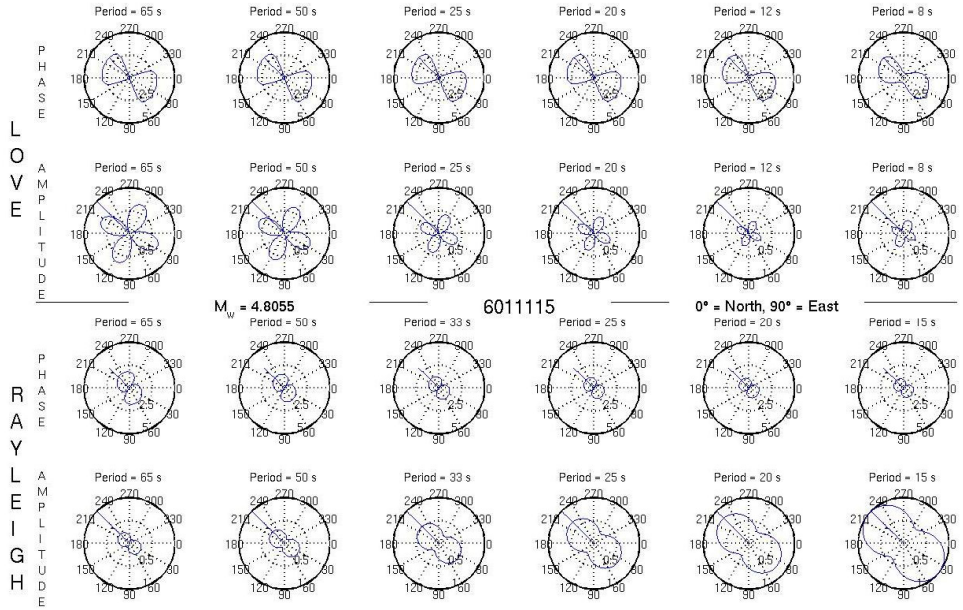

Figure B-13 Love (top) and Rayleigh (bottom) wave radiation pattern for event 6011115. The top and bottom portion of each section contains plots of the initial phase and amplitude of the seismic wave respectively. All plots are a function of period. Straight lines indicate great circle path from event epicenter to seismic station location.

FIGURE B-14. RADIATION PATTERNS

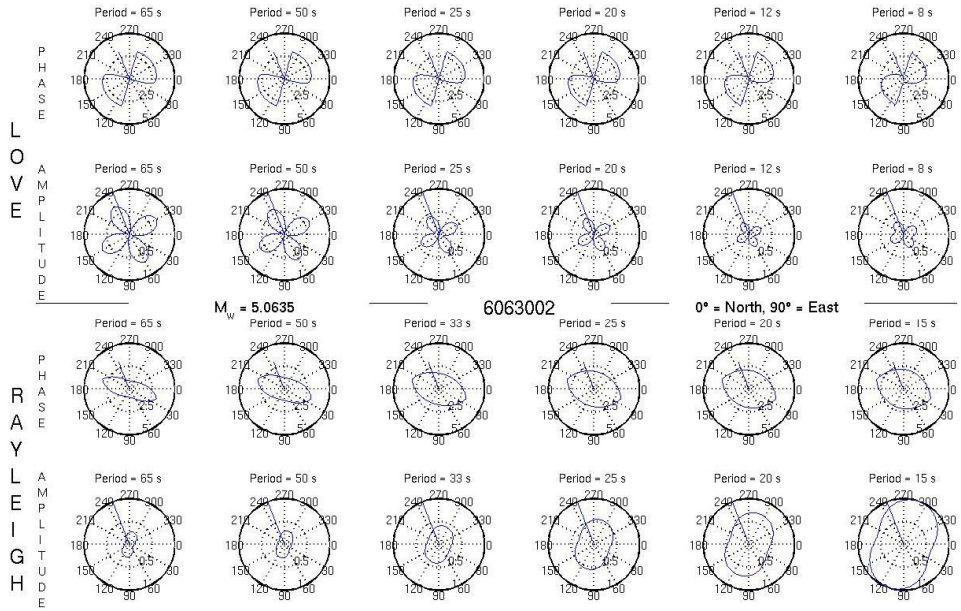

Figure B-14. Love (top) and Rayleigh (bottom) wave radiation pattern for event 6063002. The top and bottom portion of each section contains plots of the initial phase and amplitude of the seismic wave respectively. All plots are a function of period. Straight lines indicate great circle path from event epicenter to seismic station location.

FIGURE B-15. RADIATION PATTERNS

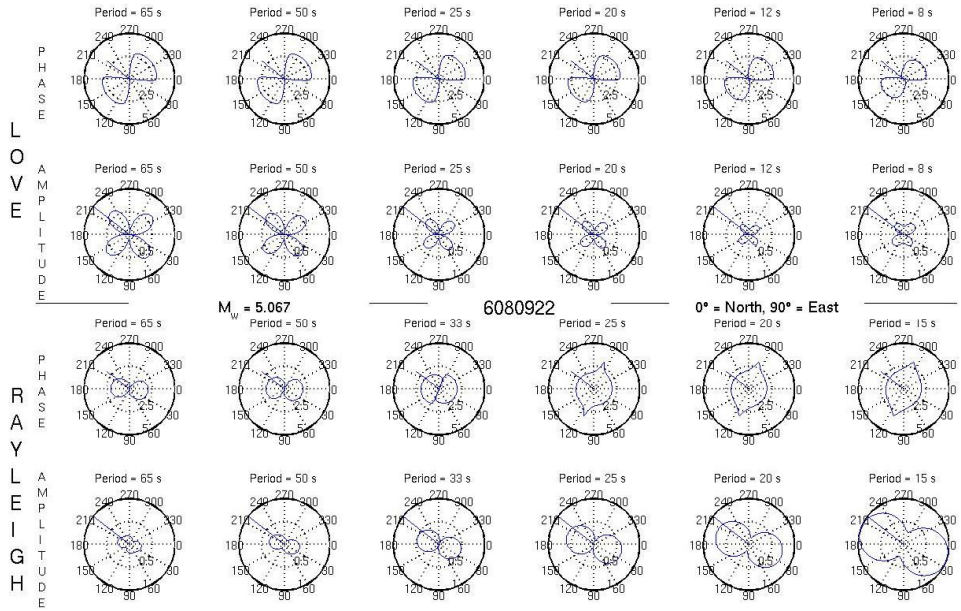

Figure B-15. Love (top) and Rayleigh (bottom) wave radiation pattern for event 6080922. The top and bottom portion of each section contains plots of the initial phase and amplitude of the seismic wave respectively. All plots are a function of period. Straight lines indicate great circle path from event epicenter to seismic station location.

FIGURE B-16. RADIATION PATTERNS

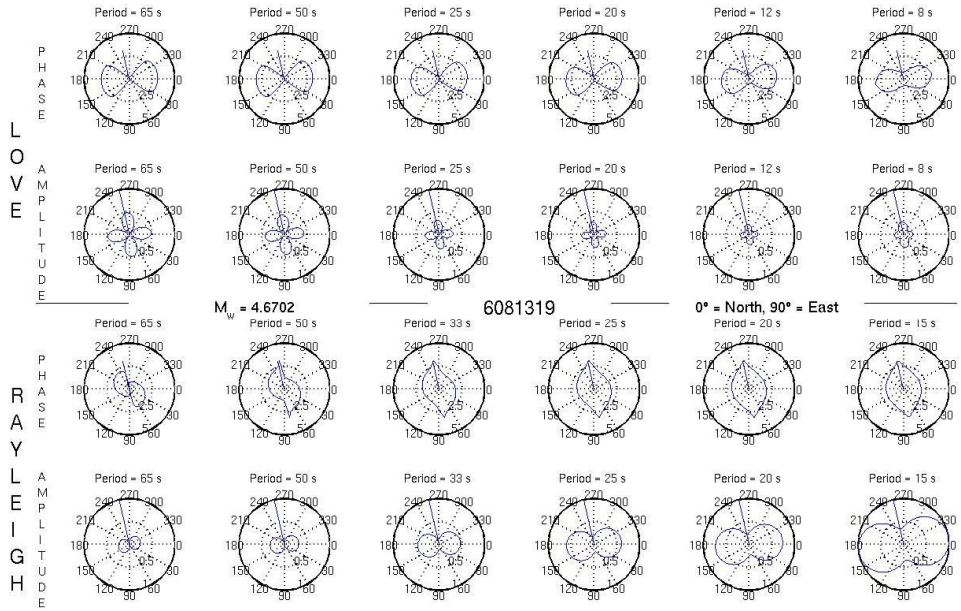

Figure B-16. Love (top) and Rayleigh (bottom) wave radiation pattern for event 6081319. The top and bottom portion of each section contains plots of the initial phase and amplitude of the seismic wave respectively. All plots are a function of period. Straight lines indicate great circle path from event epicenter to seismic station location.

FIGURE B-17. RADIATION PATTERNS

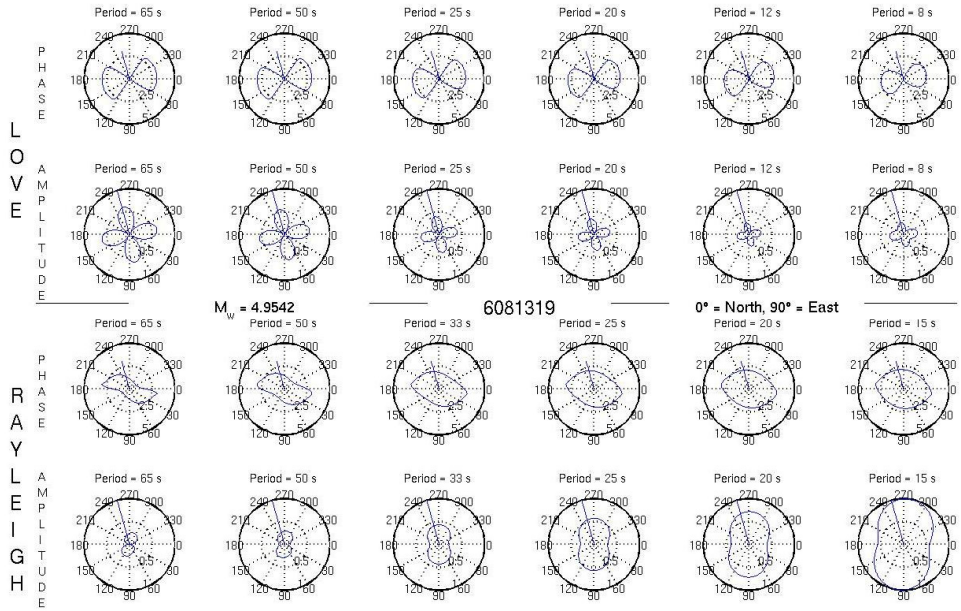

Figure B-17. Love (top) and Rayleigh (bottom) wave radiation pattern for event 6081319. The top and bottom portion of each section contains plots of the initial phase and amplitude of the seismic wave respectively. All plots are a function of period. Straight lines indicate great circle path from event epicenter to seismic station location.

FIGURE B-18. RADIATION PATTERNS

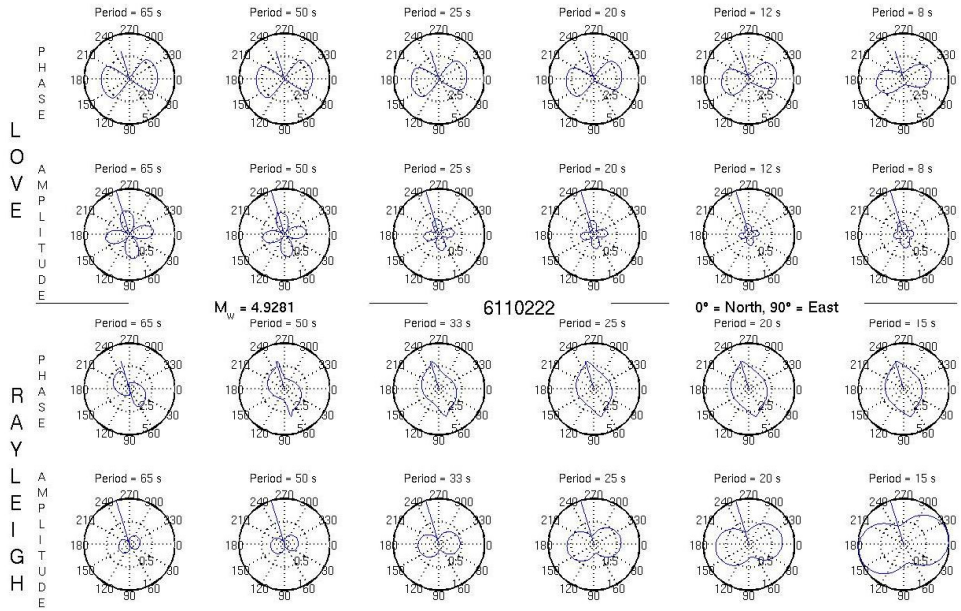

Figure B-18. Love (top) and Rayleigh (bottom) wave radiation pattern for event 6110222. The top and bottom portion of each section contains plots of the initial phase and amplitude of the seismic wave respectively. All plots are a function of period. Straight lines indicate great circle path from event epicenter to seismic station location.

FIGURE B-19. RADIATION PATTERNS

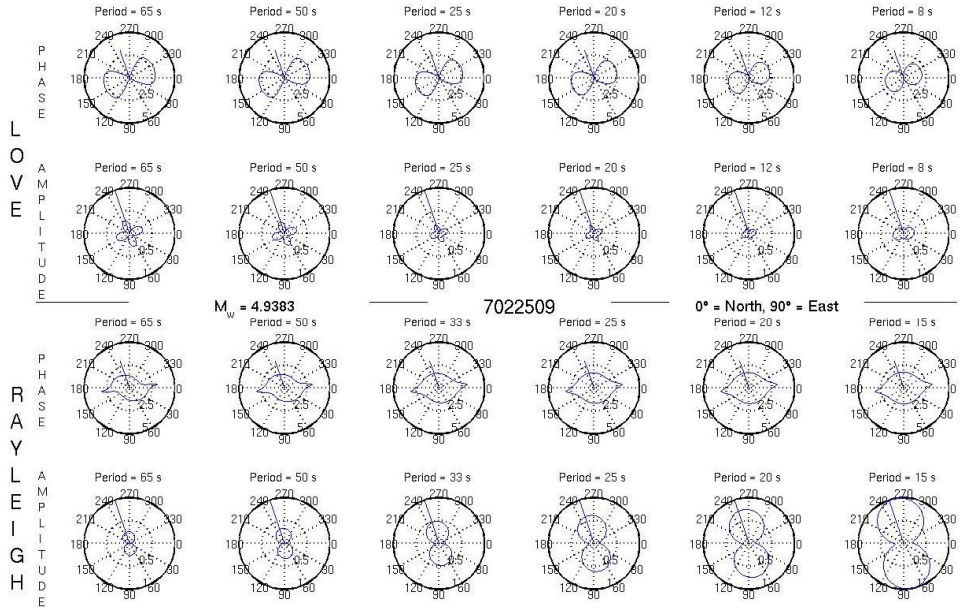

Figure B-19. Love (top) and Rayleigh (bottom) wave radiation pattern for event 7022509. The top and bottom portion of each section contains plots of the initial phase and amplitude of the seismic wave respectively. All plots are a function of period. Straight lines indicate great circle path from event epicenter to seismic station location.

FIGURE B-20. RADIATION PATTERNS

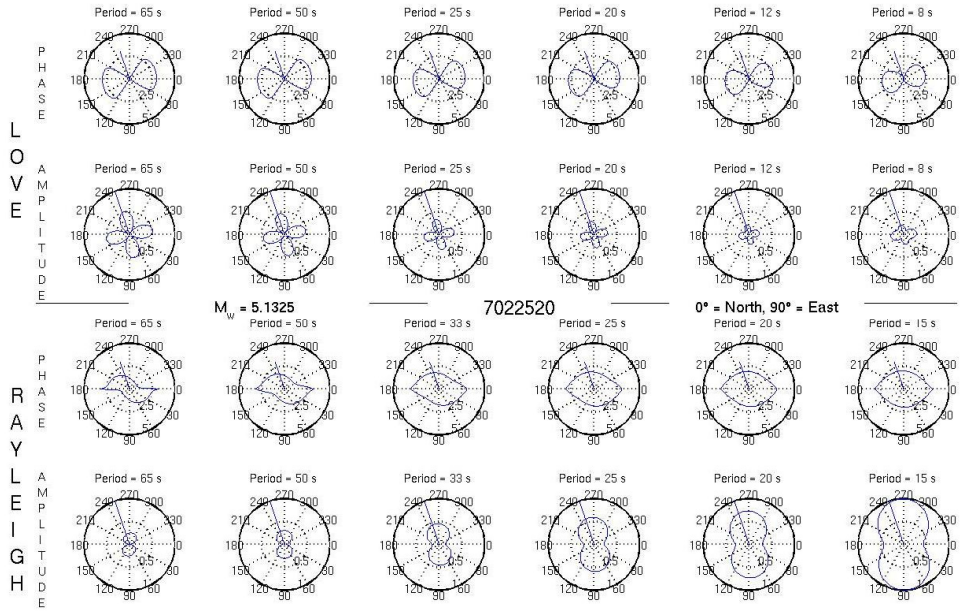

Figure B-20. Love (top) and Rayleigh (bottom) wave radiation pattern for event 7022520. The top and bottom portion of each section contains plots of the initial phase and amplitude of the seismic wave respectively. All plots are a function of period. Straight lines indicate great circle path from event epicenter to seismic station location.

FIGURE B-21. RADIATION PATTERNS

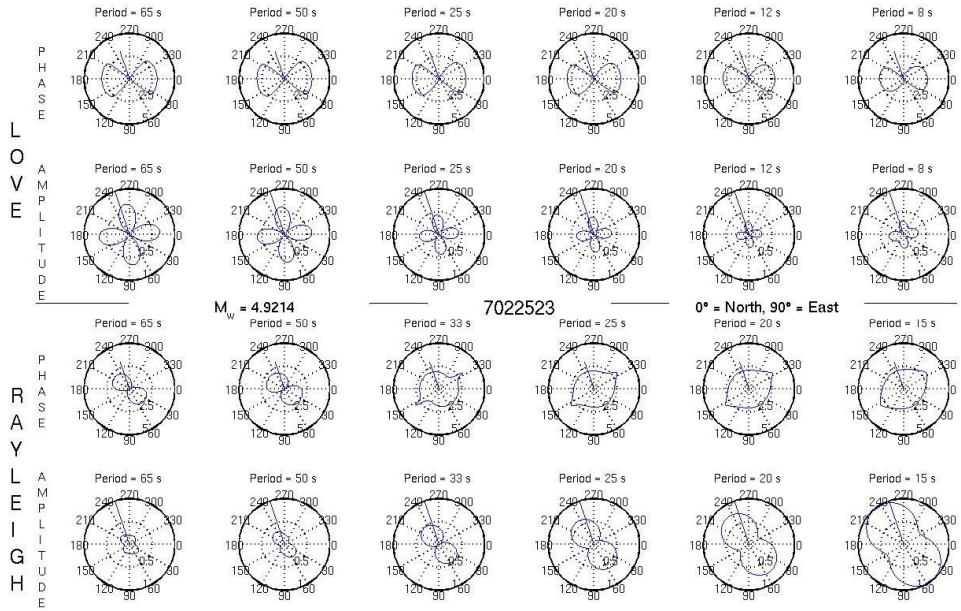

Figure B-21. Love (top) and Rayleigh (bottom) wave radiation pattern for event 7022523. The top and bottom portion of each section contains plots of the initial phase and amplitude of the seismic wave respectively. All plots are a function of period. Straight lines indicate great circle path from event epicenter to seismic station location.

FIGURE B-22. RADIATION PATTERNS

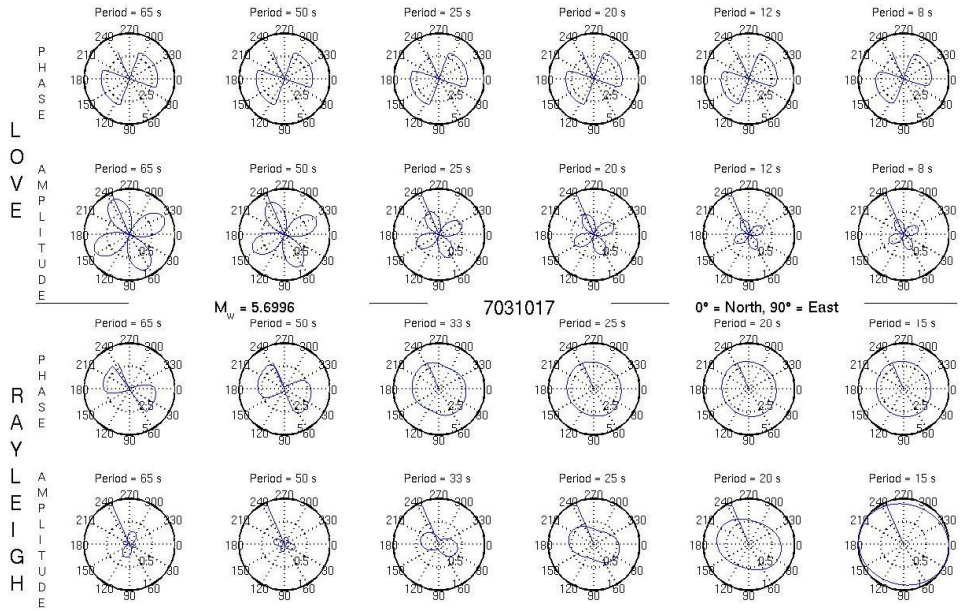

Figure B-22. Love (top) and Rayleigh (bottom) wave radiation pattern for event 7031017. The top and bottom portion of each section contains plots of the initial phase and amplitude of the seismic wave respectively. All plots are a function of period. Straight lines indicate great circle path from event epicenter to seismic station location.

FIGURE B-23. RADIATION PATTERNS

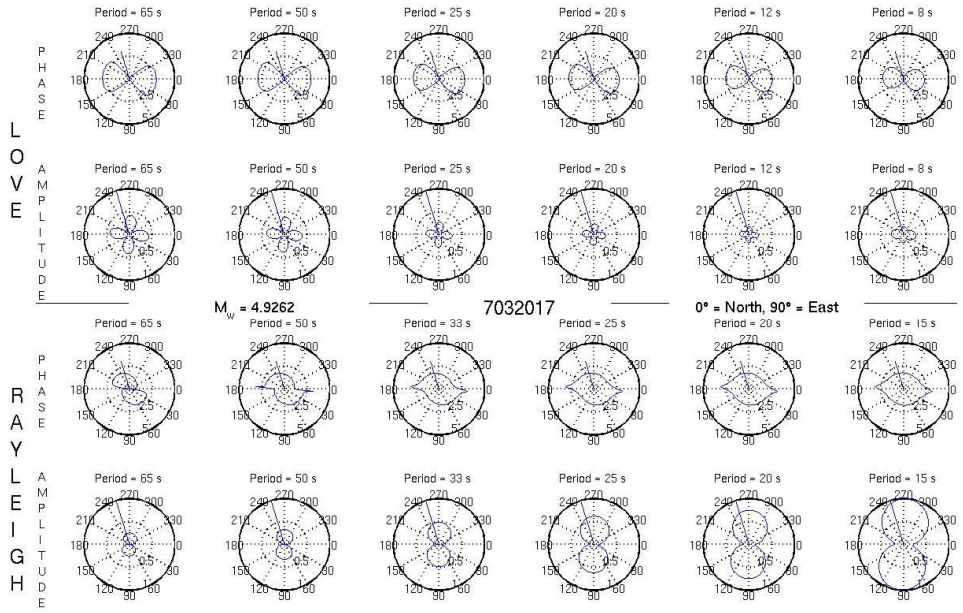

Figure B-23. Love (top) and Rayleigh (bottom) wave radiation pattern for event 7032017. The top and bottom portion of each section contains plots of the initial phase and amplitude of the seismic wave respectively. All plots are a function of period. Straight lines indicate great circle path from event epicenter to seismic station location.

FIGURE B-24. RADIATION PATTERNS

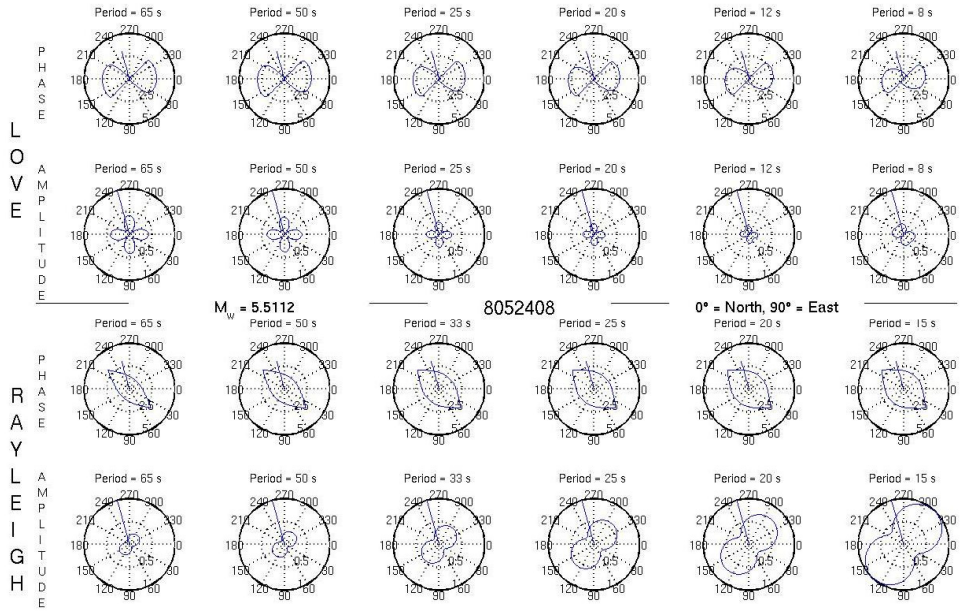

Figure B-24. Love (top) and Rayleigh (bottom) wave radiation pattern for event 8052408. The top and bottom portion of each section contains plots of the initial phase and amplitude of the seismic wave respectively. All plots are a function of period. Straight lines indicate great circle path from event epicenter to seismic station location.

FIGURE B-25. RADIATION PATTERNS

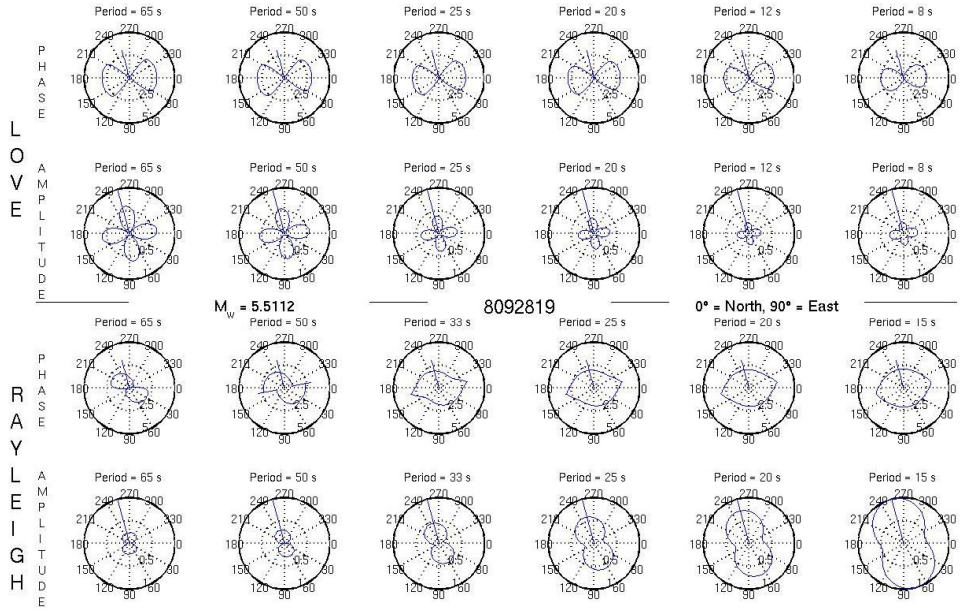

Figure B-25. Love (top) and Rayleigh (bottom) wave radiation pattern for event 8092819. The top and bottom portion of each section contains plots of the initial phase and amplitude of the seismic wave respectively. All plots are a function of period. Straight lines indicate great circle path from event epicenter to seismic station location.

FIGURE B-26. RADIATION PATTERNS

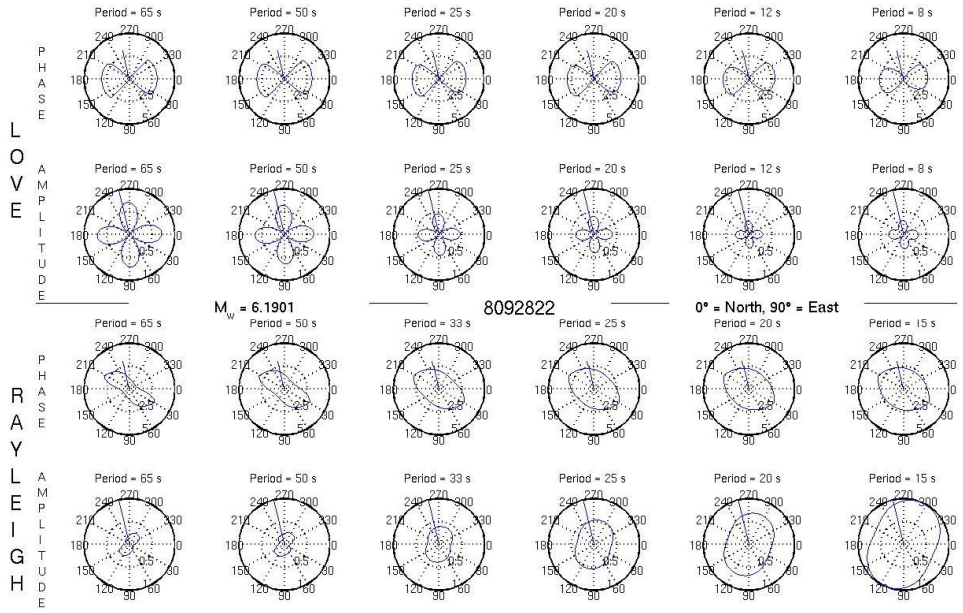

Figure B-26. Love (top) and Rayleigh (bottom) wave radiation pattern for event 8092822. The top and bottom portion of each section contains plots of the initial phase and amplitude of the seismic wave respectively. All plots are a function of period. Straight lines indicate great circle path from event epicenter to seismic station location.

FIGURE B-27. RADIATION PATTERNS

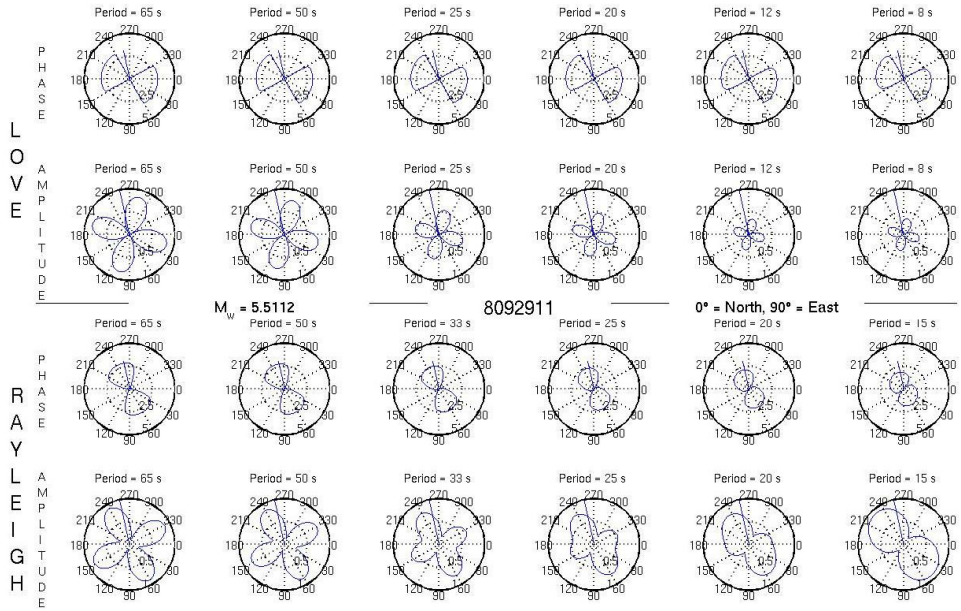

Figure B-27. Love (top) and Rayleigh (bottom) wave radiation pattern for event 8092911. The top and bottom portion of each section contains plots of the initial phase and amplitude of the seismic wave respectively. All plots are a function of period. Straight lines indicate great circle path from event epicenter to seismic station location.

FIGURE C-1. ALIGNMENT OF STATIONS JMI AND JMIC

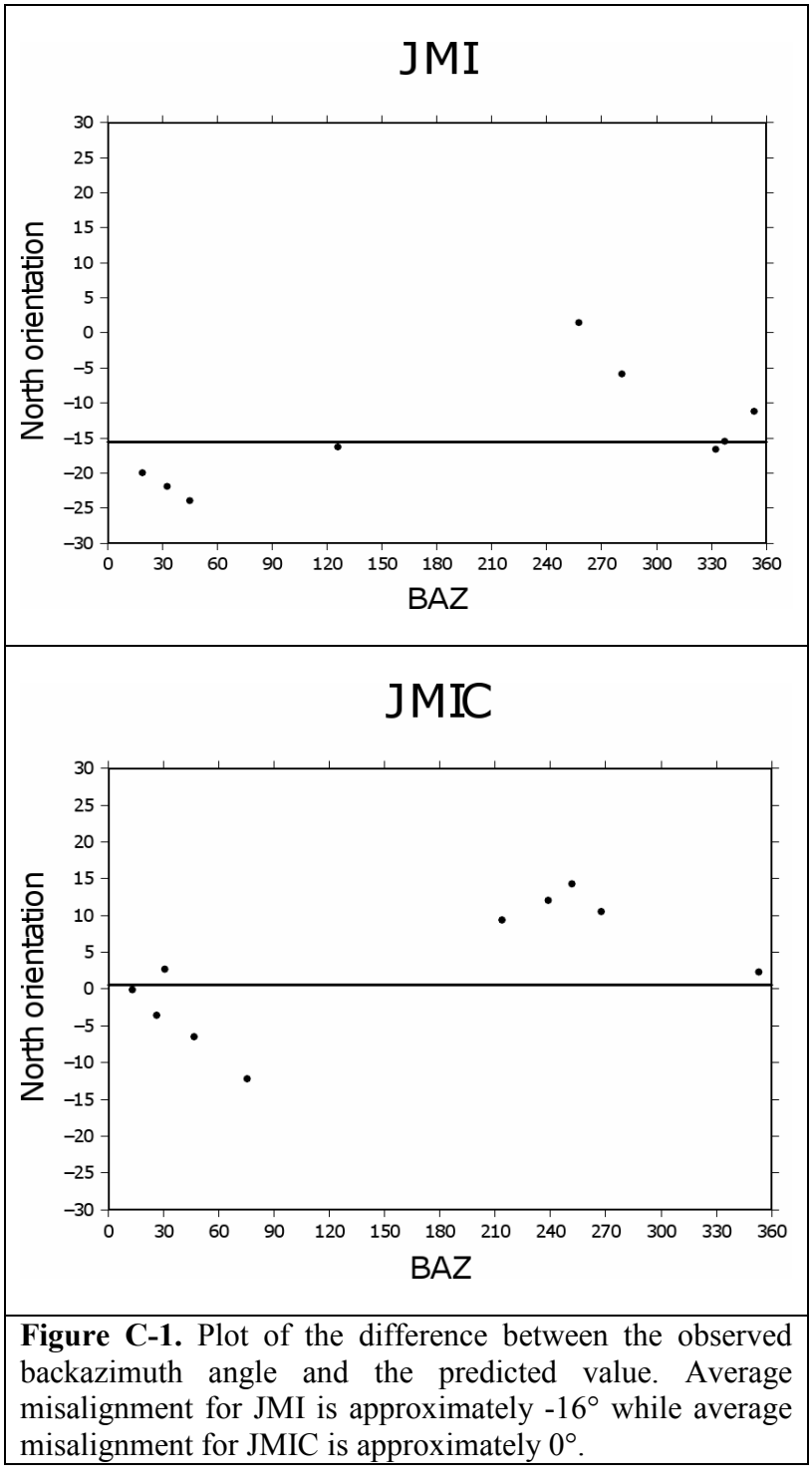

Figure C-1. Plot of the difference between the observed backazimuth angle and the predicted value. Average misalignment for JMI is approximately -16° while average misalignment for JMIC is approximately 0°.

FIGURE C-2. CROSS-CORRELATIONS

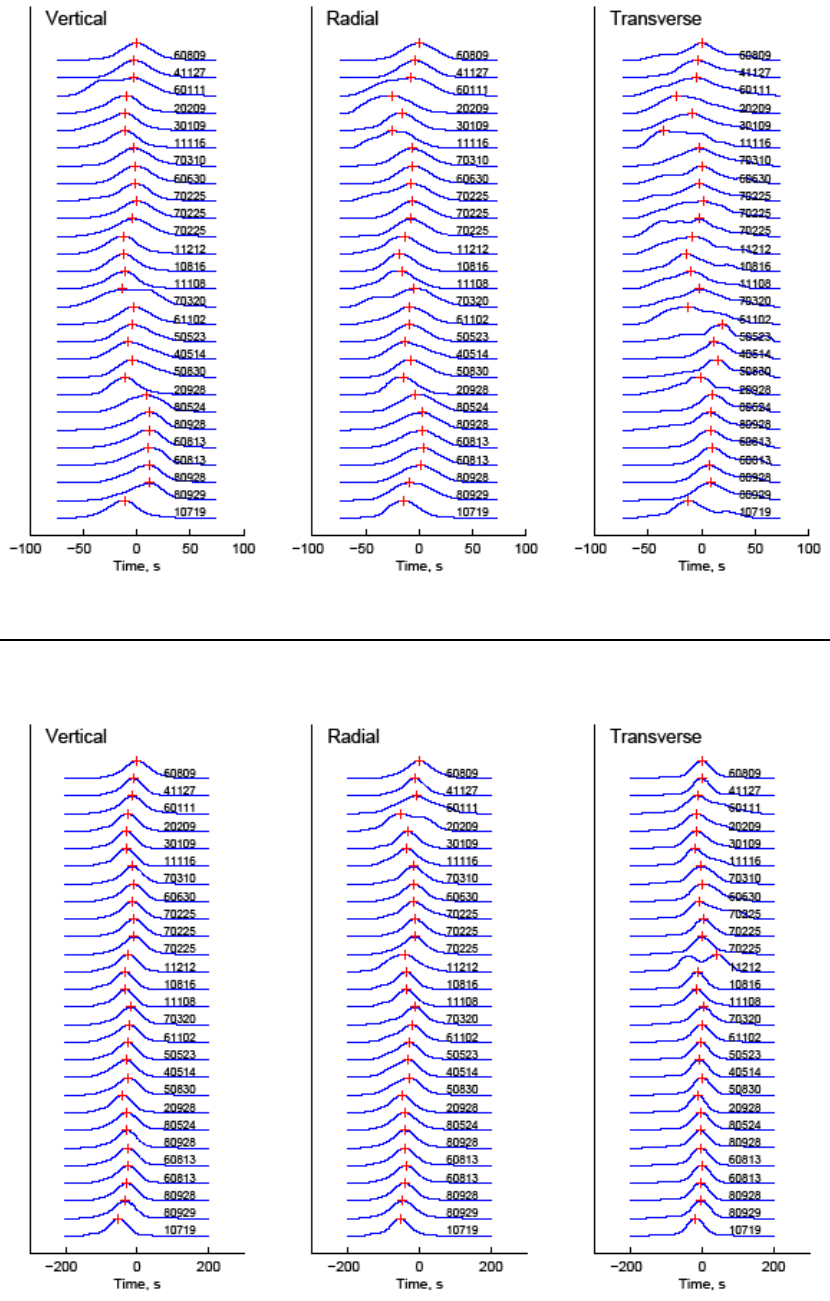

Figure C-2. Cross-correlation of the envelope of all waveforms with respect to the event furthest from the station. Waveforms are cut around the estimated P-wave (top) and S-wave (bottom) arrival times and filtered using a Gaussian filter centered at 20 s.

FIGURE C-3. PARTICLE MOTION

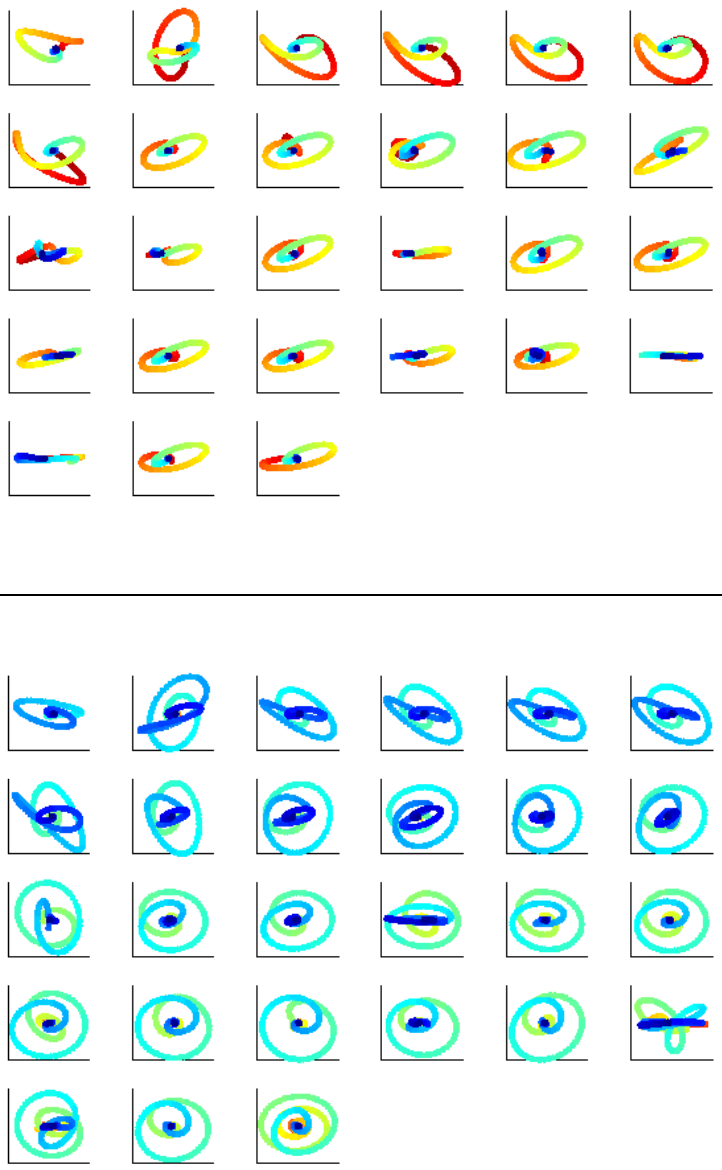

Figure C-3. Plot of radial (x-axis) versus vertical (y-axis) component of motion for each event. Waveforms are cut around the estimated P-wave (top) and S-wave (bottom) arrival times and filtered using a Gaussian filter centered at 20 s. Blue indicates initial motion while red indicates final motion.

FIGURE C-3. PARTICLE MOTION

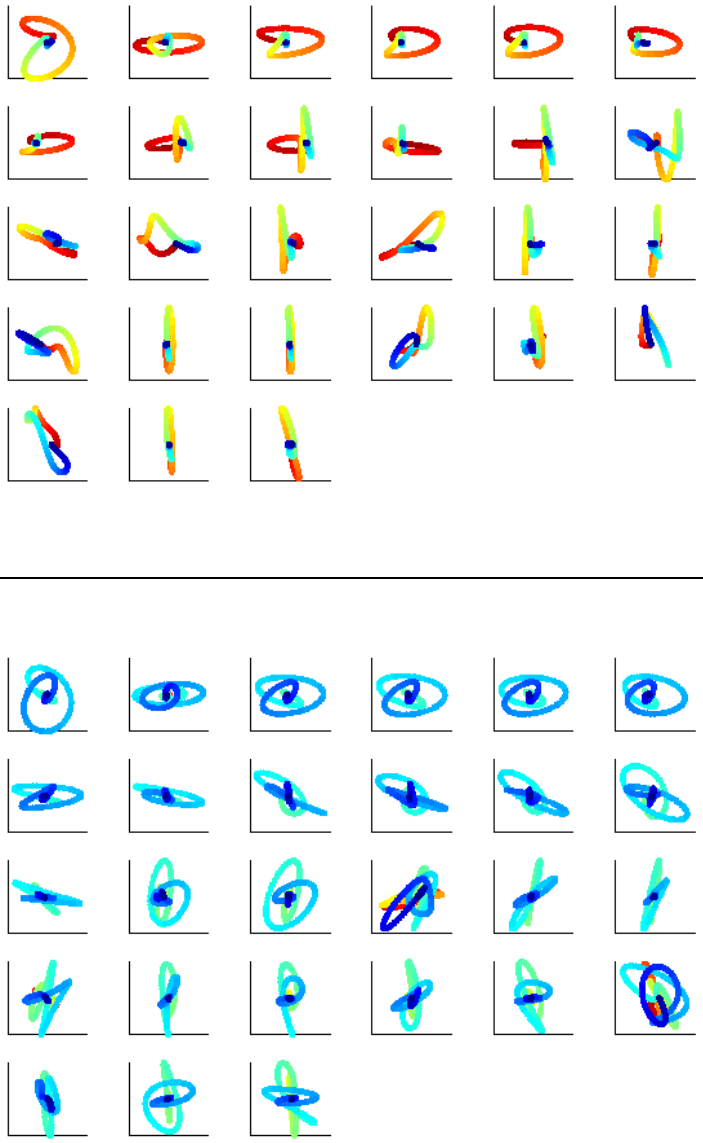

Figure C-3. Plot of transverse (x-axis) versus radial (y-axis) component of motion for each event. Waveforms are cut around the estimated P-wave (top) and S-wave (bottom) arrival times and filtered using a Gaussian filter centered at 20 s. Blue indicates initial motion while red indicates final motion.

FIGURE C-4. FREQUENCY SPECTRUM

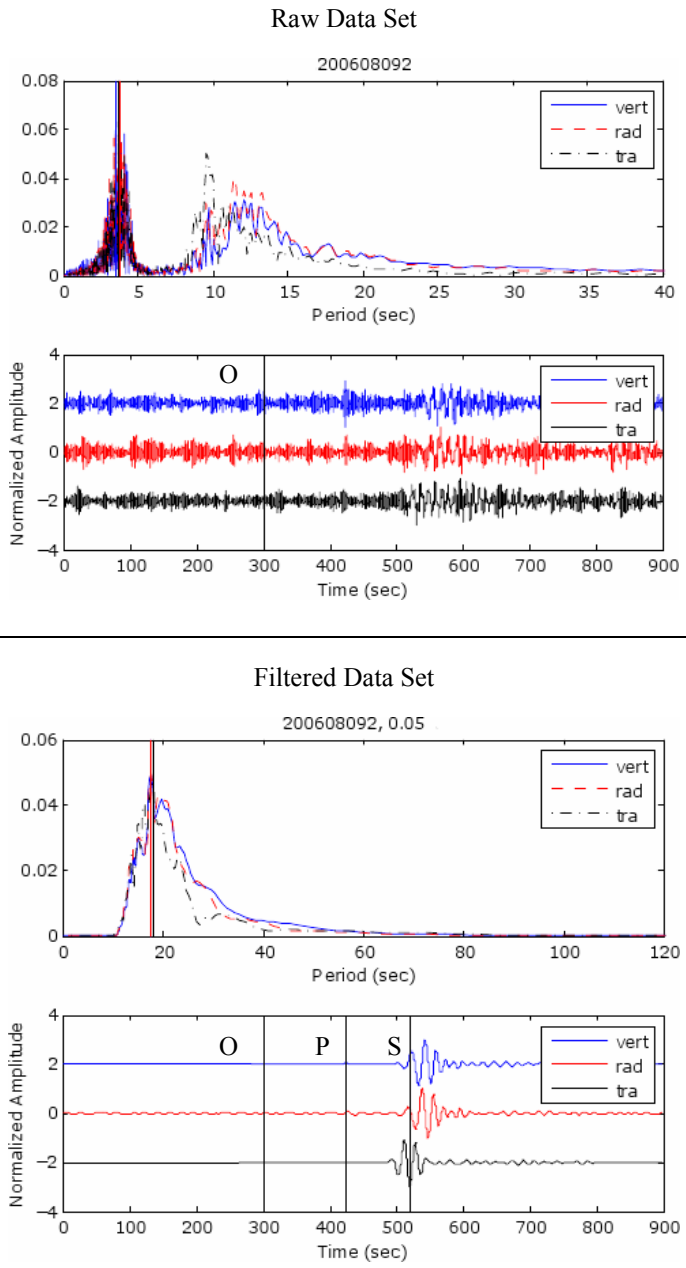

Figure C-4. Example of raw data (top figure) and data filtered at 0.05 Hz (bottom figure). Plot of frequency spectrum (upper plot) with the associated time domain seismogram (lower plot). Vertical lines in seismograms represent origin time and P/S-wave expected arrival times and are labeled accordingly.

TABLE D-1. INSTRUMENT LOCATIONS AND TYPES

TABLE D-1. INSTRUMENT INFORMATION (WWW.ORFEUS-EU.ORG)						
NETWORK	**STATION**	**START DATE**	**END DATE**	**LAT**	**LON**	**TYPE**
NNSN	JMI	1994/08/31	2003/10/31	70.93	-8.73	STS-2
NORSAR	JMIC	2003/10/31	----	70.99	-8.51	STS-2

TABLE D-2. INSTRUMENT POLES AND ZEROS

TABLE D-2. INSTRUMENT POLES AND ZEROS (HTTP://WWW.PASSCAL.NMT.EDU/INSTRUMENTATION/SENSOR/RESPONSE/STS2.HTML)				
INSTRUMENT	**POLES**	**ZEROS**	**NORMALIZING/ SCALE FACTOR**	**NATURAL PERIOD**
STS-2 (AS REPORTED BY IRIS)	-0.03701 + 0.03701i -0.03701 – 0.03701i -251.3 -131.0 + 467.3i -131.0 – 467.3i	0.00 0.00	$5.92 10^{7}$	120 S
STS-2 (JMI)	-0.03665 + 0.03739i -0.03665 -0.03739i	0.00 0.00 0.00	$1.50 10^{-6}$ $1.00 10^{6}$	
STS-2 (JMIC - BHZ)	-0.03677 + 0.03708i -0.03677 - 0.03708i -10240.96 + 2725.01i -10240.96 - 2725.01i -9512.74 + 11469.95i -9512.74 - 11469.95i -454.5256 + 0.00i -15.4294 + 0.00i -88.4672 + 396.1757i -88.4672 - 396.1757i -464.9117 + 0.00i -13338.88 + 0.00i 0.99937 + 0.00i	-461.8141 + 429.0787i -461.8141 – 429.0787i -186.7781 + 0.00i -15.1487 + 0.00i 0.00 0.00 0.00 1.00000 + 0.00i	$2.53 10^{14}$ $1.33 10^{4}$ $4.00 10^{-1}$ $1.00 10^{6}$ $9.99 10^{-1}$	

FIGURE D-1. STRECKEISEN STS-2 INSTRUMENT RESPONSE FROM MANUFACTURER

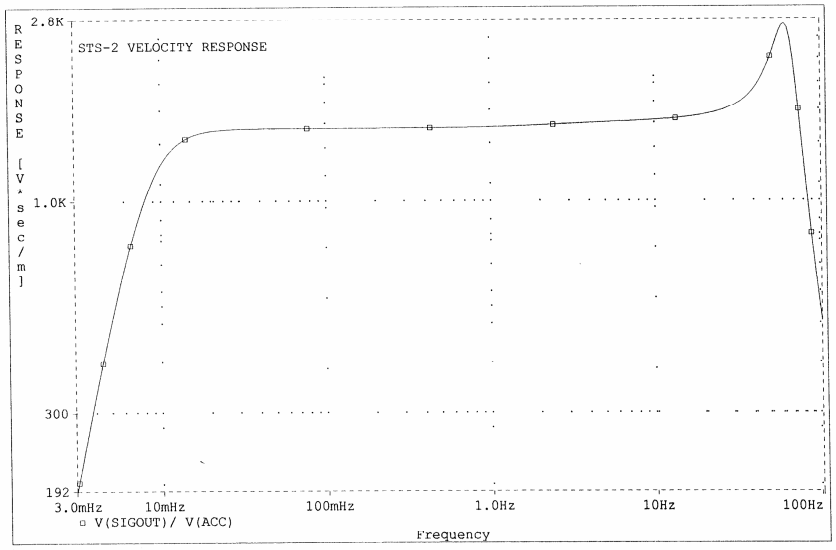

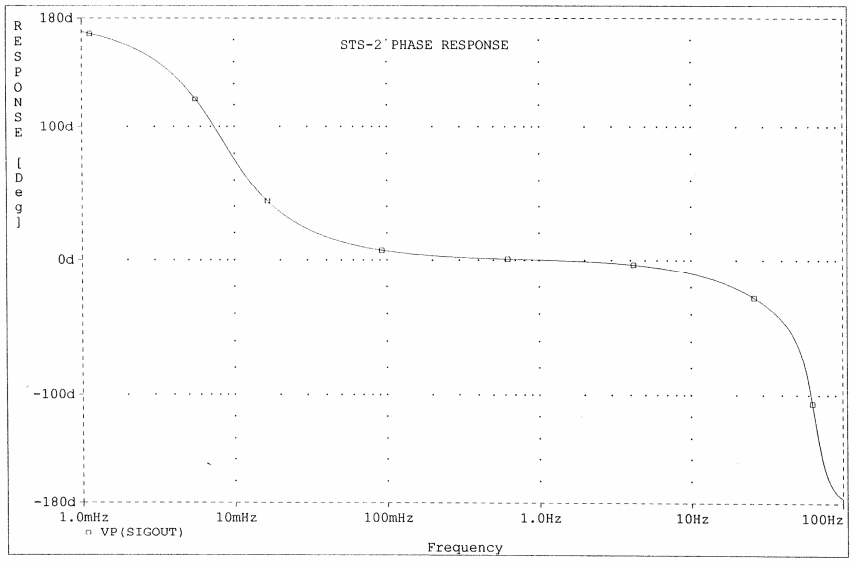

Figure D-1. Instrument response for STS-2 according to the manufacturer.

FIGURE D-2. STRECKEISEN STS-2 INSTRUMENT RESPONSE FROM POLES AND ZEROS

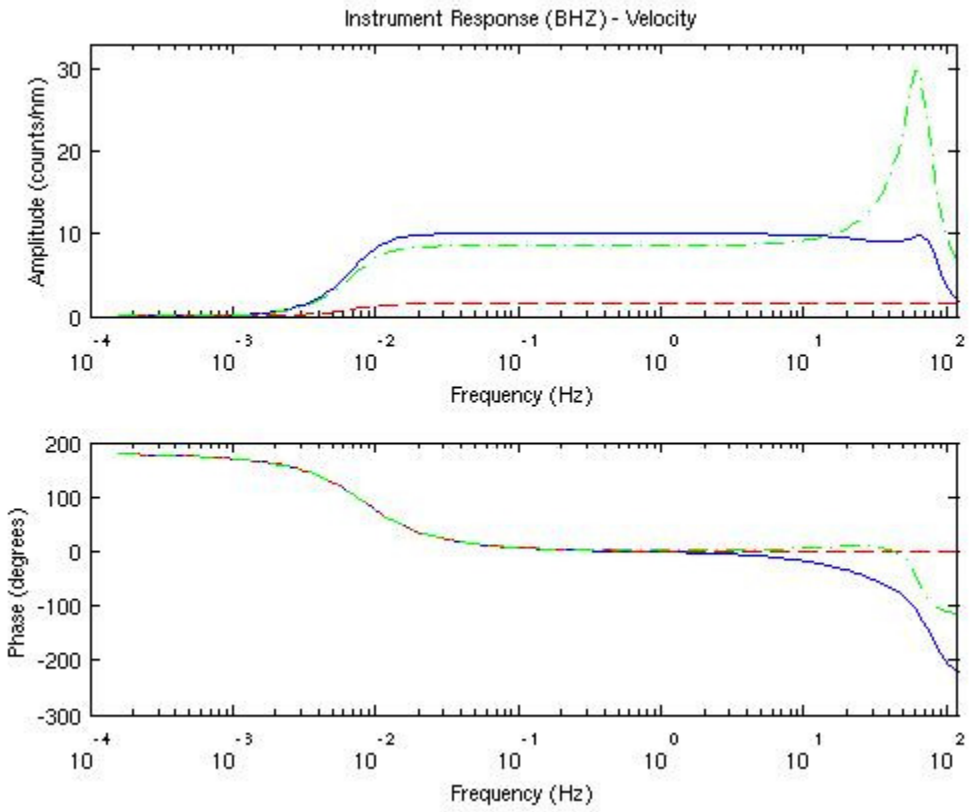

Figure D-2. Instrument response for Streckeisen STS-2, calculated using poles and zeros provided for JMI (-- red) and JMIC (-• green) compared with those provided by IRIS (blue).

FIGURE E. CODE VERIFICATION

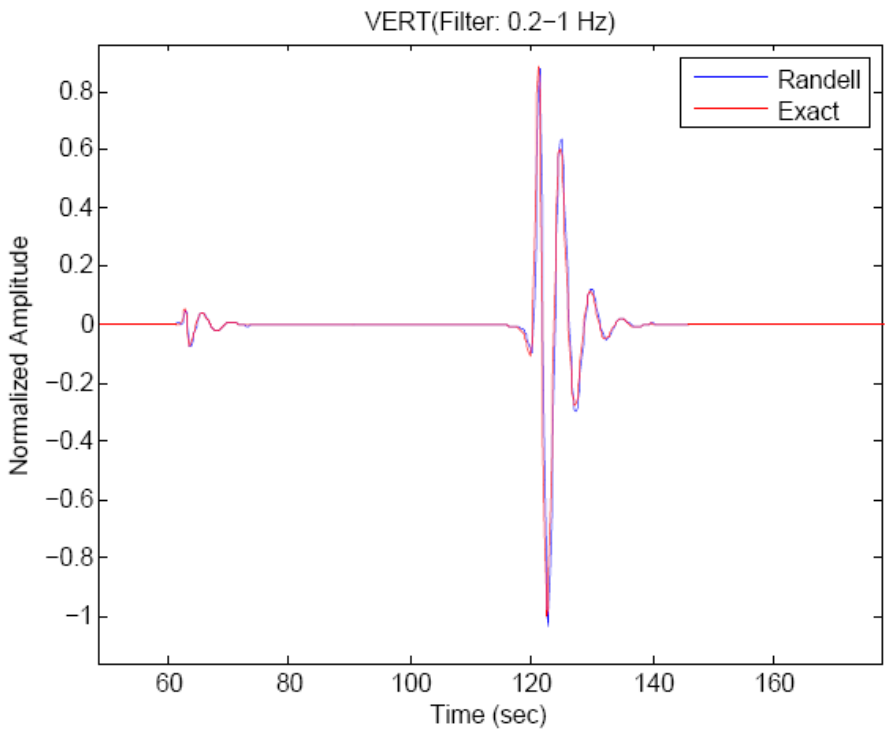

Figure E. Plot of the waveform produced by the Randall code (blue) and the exact solution of the SPICE code (red). Comparison shows excellent agreement.

TABLE F. EVENT RELOCATIONS

TABLE F. EVENT RELOCATIONS WITH BEFORE AND AFTER MISFITS FOR 26s, 34s, AND 50s DATA .

	Periods:	**26 s**		**34 s**		**50 s**	
Event #:	**Δ Range(km):**	**Misfit 1:**	**Misfit 2:**	**Misfit 1:**	**Misfit 2:**	**Misfit 1:**	**Misfit 2:**
200108160708	-7.3111	0.463	0.201	0.452	0.307	0.548	0.520
200111080200	1.2889	0.415	0.362	0.499	0.463	0.681	0.668
200112121944	9.3889	0.865	0.434	0.843	0.593	0.956	0.851
200209280236	23.289	1.449	0.321	1.334	0.553	1.151	0.812
200405140828	-16.711	0.902	0.409	0.862	0.436	0.817	0.638
200505232018	-14.111	1.072	0.386	0.879	0.541	0.928	0.808
200508302053	4.8889	0.858	0.692	0.606	0.489	0.645	0.631
200608131903	8.5889	1.266	0.908	0.933	0.728	0.785	0.819
200608131943	-7.3111	1.379	1.142	0.850	0.830	0.714	0.705
200611022252	-14.611	1.196	0.993	0.841	0.625	0.721	0.633
200702250913	-14.711	1.042	0.433	0.722	0.422	0.610	0.531
200702252013	-7.0111	0.459	0.375	0.454	0.392	0.610	0.582
200702252312	-5.7111	0.373	0.425	0.426	0.433	0.619	0.590
200703201703	6.7889	0.658	0.378	0.699	0.487	0.881	0.691
200805240818	19.689	1.649	0.689	1.276	0.824	1.053	1.038
200809281952	10.589	1.233	0.740	0.937	0.683	0.821	0.842
200809282220	5.5889	1.344	1.168	1.006	0.927	0.955	1.010
200809291103	-2.6111	0.671	0.540	0.619	0.635	0.771	0.822

FIGURE F. EVENT RELOCATIONS

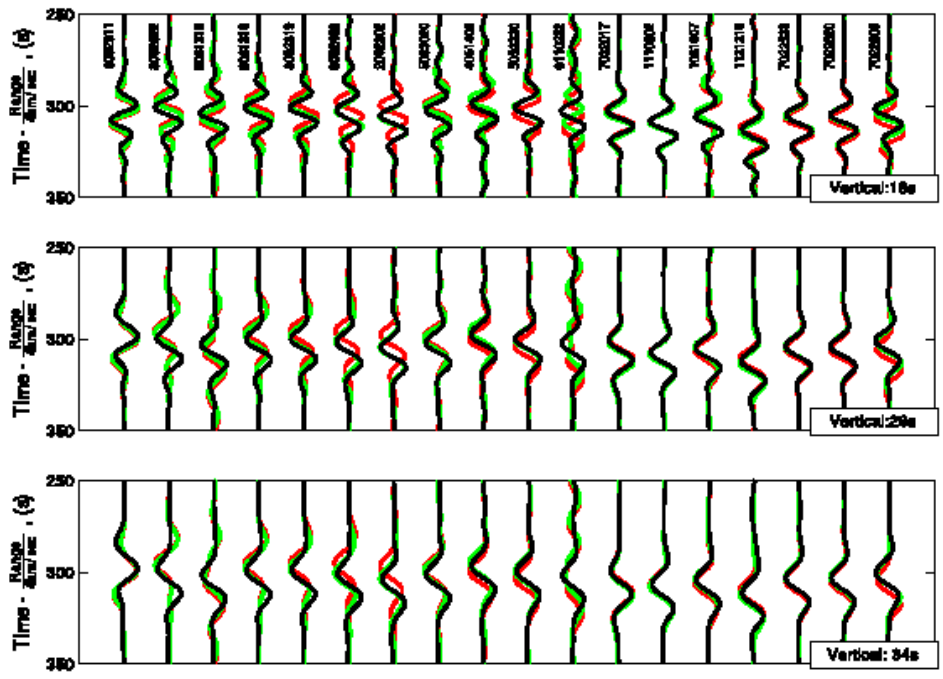

Figure F. Comparison of the vertical component of the recorded data (black), the vertical component of the synthetic waveform created at the original epicenter (red), and the vertical component of the synthetic waveform created at the relocated epicenter (green) for 18 s, 26 s, and 34 s data.

REFERENCES

Aki, K. and P. G. Richards (2002), *Quantitative Seismology, 2nd edition*, University Science Books, Sausalito, California.

Bijwaard, H. and W. Spakman (1999), Tomographic evidence for a narrow whole mantle plume below Iceland, *Earth and Planetary Science Letters*, 166, 121-126.

Blackman, D. K., C. E. Nishimura and J. A. Orcutt (2000), Seismoacoustic recordings of a spreading episode on the Mohns Ridge, *Journal of Geophysical Research*, 105, 10,961-10,973.

Bozdag, E. and J. Trampert (2008), On crustal corrections in surface wave tomography, *Geophysical Journal International*, 172, 1066-1082.

Bown, J. W. and R. S. White (1994), Variation with spreading rate of oceanic crustal thickness and geochemistry, *Earth and Planetary Science Letters*, 121, 435-449.

Cannat, M. (1996), How thick is the magmatic crust at slow spreading oceanic ridges, *Journal of Geophysical Research*, 101, 2847-2857.

Delorey, A. A., R. A. Dunn, and J. B. Gaherty (2007) Surface wave tomography of the upper mantle beneath the Reykjanes Ridge with implications for ridge-hot spot interaction, *Journal of Geophysical Research*, 112, B08313, doi:10.1029/2006JB004785.

Dick, H. J. B., J. Lin, and H. Schouten (2003), An ultraslow-spreading class of ocean ridge, *Nature*, 426, 405-412.

Dunn, R. A., and D. R. Toomey (2001), Crack-induced seismic anisotropy in the oceanic crust across the East Pacific Rise (9°30'N), *Earth and Planetary Science Letters*, 189, 9-17.

Dunn, R. A., and D. W. Forsyth (2003), Imaging the transition between the region of mantle melt generation and the crustal magma chamber beneath the southern East Pacific Rise with short-period Love waves, *Journal of Geophysical Research*, 108(B7), 2352, doi:10.1029/2002JB002217.

Ekström, G., A. M. Dziewonski, N. N. Maternovskaya, and M. Nettles (2005), Global seismicity of 2003: Centroid-moment-tensor solutions for 1087 earthquakes, *Physics of the Earth and Planetary Interiors*, 148(2-4), 327-351.

Faul, U. and I. Jackson (2005), The seismological signature of temperature and grain size variations in the upper mantle, *Earth and Planetary Science Letters*, 234, 119-134.

Francis, T. J. (1981), Serpentinization faults and their role in the tectonics of slow spreading ridges, *Journal of Geophysical Research*, 86, 11616-11622.

Gaherty, J. B. (2001), Seismic Evidence for Hotspot-Induced Buoyant Flow Beneath the Reykjanes Ridge, *Science*, 293, 1645-1647.

Gaherty, J. B., and R. A. Dunn (2007), Evaluating hot spot – ridge interaction in the Atlantic from regional-scale seismic observations, *Geochemistry, Geophysics, Geosystems*, 8, Q05006, doi:10.1029/2006GC001533.

Géli, L. (1993), Volcano-tectonic events and sedimentation since Late Miocene times at Mohns ridge, near 72°N, in the Norwegian-Greenland sea, *Tectonophysics*, 222, 417-444.

Géli, L., V. Renard and C. Rommevaux (1994), Ocean crust formation processes at very slow spreading centers: A model for the Mohns Ridge, near 72°N, based on magnetic, gravity, and seismic data, *Journal of Geophysical Research*, 99, 2995-3013.

Goldstein, P. (1996), SAC2000: Seismic signal processing and analysis tools for the 21st century, *Seismological Research Letters*, 67, 39.

Gu, Y. J., S. C. Webb, A. Lerner-Lam, and J. B. Gaherty (2005), Upper mantle structure beneath the eastern Pacific Ocean ridges, *Journal of Geophysical Research*, 110, B06305, doi:10.1029/2004JB003381.

Haase, K. M., C. W. Devey, D. F. Mertz, P. Stoffers, and D. Garbe-Schonberg (1996), Geochemistry of lavas from Mohns Ridge, Norwegian-Greenland Sea: implications for melting conditions and magma sources near Jan Mayen, *Contributions to Mineralogy and Petrology*, 123, 223-237.

Hanan, B. B., J. Blichert-Toft, R. Kingsley, and J.-G. Schilling (2000), Depleted Iceland mantle plume geochemical signature: Artifact of multicomponent mixing?, *Geochemistry, Geophysics, Geosystems*, 1, doi:10.1029/1999GC000009.

Jackson, H. R., I. Reid, R. K. H. Falconer (1982), Crustal structure near the Arctic mid-ocean ridge, *Journal of Geophysical Research*, 87, 1773-1783.

Jakobsson, M., R. Macnab, L. Mayer, R. Anderson, M. Edwards, J. Hatzky, H.-W. Schenke, and P. Johnson (2008), An improved bathymetric portrayal of the Arctic Ocean: Implications for ocean modeling and geological, geophysical and oceanographic analyses, *Geophysical Research Letters*, 35, doi:10.1029/2008GL033520

Jokat, W., O. Ritzmann, M. C. Schmidt-Aursch, S. Drachev, S. Gauger and J. Snow (2003), Geophysical evidence for reduced melt production on the Artic ultraslow Gakkel mid-ocean ridge, *Nature*, 423, 962-965.

Klingelhöfer, F., L. Géli, L. Matias, N. Steinsland and J. Mohr (2000a), Crustal structure of a super-slow spreading centre: a seismic refraction study of Mohns Ridge, 72°N, *Geophysical Journal International*, 141, 509-526.

Klingelhöfer, F., L. Géli, R. S. White (2000b), Geophysical and geochemical constraints on crustal accretion at the very-slow spreading Mohns Ridge, *Geophysical Research Letters*, 27, 1547-1550.

Kreemer, C., W. E. Holt and A. J. Haines (2003), An integrated global model of present-day plate motions and plate boundary deformation, *Geophysical Journal International*, 154, 8-34.

Lizarralde, D, J. B. Gaherty, J. A. Collins, G. Hirth and S. D. Kim (2004), Spreading-rate dependence of melt extraction at mid-ocean ridges from mantle seismic refraction data, *Nature*, 432, 744-746.

Michael, P. J., C. H. Langmuir, H. J. Dick, J. E. Snow, S. L. Goldstein, D. W. Graham, K. Lehnert, G. Kurras, W. Jokat, R. Mühe, and H. N. Edmonds (2003), Magmatic and amagmatic seafloor generation at the ultraslow-spreading Gakkel Ridge, Arctic Ocean, *Nature*, 423, 961-965.

Muller, M. R., C. J. Robinson, T. A. Minshull, R. S. White and M. J. Bickle (1997), Thin crust beneath ocean drilling program borehole 735B at the Southwest Indian Ridge?, *Earth and Planetary Science Letters*, 117, 295-317.

Muller, R. D., M. Sdrolias, C. Gaina and W. R. Roest (2008), Age, spreading rates, and spreading asymmetry of the world's ocean crust, *Geochemistry Geophysics Geosystems*, 9, Q04006, doi:10.1029/2007GC001743.

Neumann, E.-R. and J. G. Schilling (1984), Petrology of basalts from the Mohns-Knipovich Ridge: The Norwegian-Greenland Sea, *Contributions to Mineralogy and Petrology*, 85, 204-233.

Nishimura, C. E. and D. W. Forsyth (1989), The anisotropic structure of the upper mantle in the Pacific, *Geophysical Journal*, 96, 203-229.

Niu, Y. and R. Hekinian (1997), Spreading-rate dependence of the extent of mantle melting beneath ocean ridges, *Nature*, 385, 326-329.

Nolet, G. (2008), *A Breviary of Seismic Tomography: Imaging the Interior of the Earth and Sun*, Cambridge University Press, Cambridge, UK.

Phipps Morgan, J. and Y. J. Chen (1993), Dependence of ridge-axis morphology on magma supply and spreading rate, *Nature*, 364, 706-708.

Pilidou, S., K. Priestley, E. Debayle and O. Gudmundsson (2005), Rayleigh wave tomography in the North Atlantic: high resolution images of the Iceland, Azores and Eifel mantle plumes, *LITHOS*, 79, 453-474.

Pilidou, S., K. Priestley, O. Gudmundsson and E. Debayle (2004), Upper mantle *S*-wave speed heterogeneity and anisotropy beneath the North Atlantic from regional surface wave tomography: the Iceland and Azores plumes, *Geophysical Journal International*, 159, 1057-1076.

Randall, G. E. (1994), Efficient calculation of complete differential seismograms for laterally homogeneous earth models, *Geophysical Journal International*, 118, 245-254.

Reid, I., and H. R. Jackson (1981), Oceanic spreading rate and crustal thickness, *Marine Geophysical Researches*, 5, 165-172.

Ritzmann O., W. Jokat, R. Mjelde, and H. Shimamura (2002), Crustal structure between the Knipovich Ridge and the Van Mijenfjorden (Svalbard), *Marine Geophys. Res.*, 23(5-6), 379-401.

Scherbaum, F. (2001), *Of Poles and Zeros: Fundamentals of Digital Seismology, 2nd Edition*, Kluwer Academic Publishers, Dordrecht, Netherlands.

Schilling, J.-G. (1985), Upper mantle heterogeneities and dynamics, *Nature*, 314, 65-67.

Schilling, J.-G, R. Kingsley, D. Fontignie, R. Poreda, and S. Xue (1999), Dispersion of the Jan Mayen and Iceland mantle plumes in the Arctic: A He-Pb-Nd-Sr isotope tracer study of basalts from the Kolbeinsy, Mohns, and Knipovich Ridges, *Journal of Geophysical Research*, 104, 10,543-10,569.

Schmeling, H. (1985), Numerical models on the influence of partial melt on elastic, anelastic, and electrical properties of rocks, part I: Elasticity and anelasticity, *Phys. Earth Planet. Inter.*, 41, 34-57.

Schroeder, T., B. John, and B. R. Frost (2002), Geologic implications of seawater circulation through peridotite exposed at slow-spreading mid-ocean ridges, *Geology*, 30, 367-370.

Stein, S. and M. Wysession (2003), *An Introduction to Seismology, Earthquakes, and Earth Structures*, Blackwell Publishing Ltd., Malden, Massachusetts.

Talwani, M. and O. Eldholm (1977), Evolution of the Norwegian-Greenland Sea, *Geological Society of America Bulletin*, 88, 969-999.

Turcotte, D. L., and G. Schubert (2002), *Geodynamics*, Cambridge University Press, Cambridge, U.K.

Vogt, P. R. (1986), Geophysical and geochemical signatures and plate tectonics, *The Nordic Sea*, ed. B. G. Hurdle, pp 413-628, Springer-Verlag, New York.

Vogt, P. R., R. K. Perry, R. H. Feden, H. S. Fleming and N. Z. Cherkis (1981), The Greenland-Norwegian Sea and Iceland environment: Geology and geophysics, *The Arctic Ocean, vol. 5*, ed. B. G. Hurdle, pp 493-598, Springer-Verlag, New York.

Weins, D. A., K. A. Kelley, and T. Plank (2006), Mantle temperature variations beneath back-arc spreading centers inferred from seismology, petrology, and bathymetry, *Earth and Planetary Science Letters*, 243, 30-42.

Wessel, P., and W. H. Smith (1998), New, improved version of the Generic Mapping Tools released, *Eos Transactions AGU*, 79,579.

Xu, Y. and D. A. Weins (1997), Upper mantle structure of the southwest Pacific from regional waveform inversion, *Journal of Geophysical Research*, 102, 27,439-27,451.

Yomogida, K. and K. Aki (1985), Waveform synthesis of surface waves in a laterally heterogeneous Earth by the Gaussian beam method, *Journal of Geophysical Reasearch*, 90, 7665-7688.

Zhang, Y.-S. and T. Tanimoto (1992), Ridges, hotspots and their interaction as observed in seismic velocity maps, *Nature*, 355, 45-49.

Zhao, D (2004), Global tomographic images of mantle plumes and subducting slabs: insight into deep Earth dynamics, *Physics of the Earth and Planetary Interiors*, 146, 3-34.